Summer 8-10-2016

Experimental Study and Numerical Simulation of Methane Oxygen Combustion inside a Low Pressure Rocket Motor

mine kaya
University of New Orleans, mkaya@uno.edu

Experimental Study and Numerical Simulation of Methane Oxygen Combustion inside a Low Pressure Rocket Motor

A Thesis

Submitted to the Graduate faculty of
University of New Orleans
in partial fulfillment of the
requirements for the degree of

Master of Science
In
Mechanical Engineering
Thermal Fluids Science

by

Mine Kaya

B.Sc., Middle East Technical University, 2012

August, 2016

Dedicated to my family

Acknowledgements

First of all, I would like to emphasize the contribution from my supervisor Dr. Kazim M. Akyuzlu. This work would not have been accomplished without his invaluable guidance and encouragement. I would also like to thank Dr. Martin J. Guillot, Dr. Paul Herrington and Dr. Paul Schilling for serving on my thesis committee.

I am grateful to my classmates Seda, Amer and Jose for their friendship, encouragement and help throughout this year.

This research was supported in part by NASA EPSCoR and Board of Regents Support Fund / NASA(2014)-RAP-09

TABLE OF CONTENTS

NOMENCLATURE

Symbols

A	Absorption coefficient
A	Empirical constant
A_r	Pre-exponential factor
B	Empirical constant
C	Constant, molar concentration
c_p	Specific heat
D	Diffusion coefficient, energy transfer due to species diffusion
E_r	Activation energy
G	Incident radiation
J	Diffusion flux of species
K	Thermal conductivity, turbulent kinetic energy
k_f	Arrhenius rate
M	Molecular mass
N	Refractive index
P	Pressure
Pr	Prandtl number
R	Production rate of species
R	Universal gas constant
S	Modulus of the mean rate of strain tensor
Sc	Schmidt number
T	Time
T	Temperature
U	Velocity in x direction
V	Velocity in y direction
V	Velocity
Y	Mass fraction

Greek Symbols

E	Turbulence dissipation rate
H	Rate exponent
M	Viscosity
N	Stoichiometric coefficient
Φ	Viscous dissipation
P	Density
Σ	Stefan-Boltzmann constant

Subscripts

Eff	Effective
F	Fuel
Gen	Generation
i, j	Index
In	Inlet
M	Mass
O	Outlet
Ox	Oxidizer
R	Radiative
T	Turbulent
T	Thermal

Superscripts

P	Product
R	Reactant

TABLE OF TABLES

TABLE OF FIGURES

ABSTRACT

In this thesis, combustion processes in a laboratory-scale methane based low pressure rocket motor (LPRM) is studied experimentally and numerically. Experiments are conducted to measure flame temperatures and chamber temperature and pressure. Single reaction-four species reacting flow of gaseous methane and gaseous oxygen in the combustion chamber is also simulated numerically using a commercial CFD solver based on 2-D, steady-state, viscous, turbulent and compressible flow assumptions. LPRM geometry is simplified to several configurations, i.e. Channel and Combustion Chamber with Nozzle and FWD. Flow in a Bunsen burner is simulated inside Channel geometry in order to validate the reaction model. Grid independence study is also conducted for reacting as well as non-reacting flows. Numerical model is calibrated based on experimental results. Results of the computational model are found in a good agreement with the experimental data after calibrating specific heats of the products. Parametric study is conducted in order to investigate the effects of different mass flow rates and chamber pressures on flow and combustion characteristics of a LPRM to provide insight to future studies.

Keywords: Low Pressure Rocket Motor, Methane oxygen combustion

1. INTRODUCTION

Methane has been one of the most widely used fuel since Industrial Revolution. With the recent advancements in the rocket engine technology, combustion of methane seems to remain as an important research area. SpaceX is developing a methane-based rocket engine for the spaceship, called Mars Colonial Transporter (MCT) [1], [2].

In the present study, combustion processes inside a laboratory-scale low pressure rocket motor (LPRM) is studied both experimentally and numerically. The existing low pressure hybrid rocket motor setup [3] which is developed for combustion studies at the University of New Orleans Combustion Laboratory is used for the present study after the combustion chamber was modified in order to carry on the experiments for methane – based LPRM.

The aim of this study is to develop a mathematical model for the reacting flow of methane and oxygen inside a combustion chamber of LPRM and calibrate this model based on the experimental data. The calibrated computational model will provide insight to the future studies.

The reacting flow of methane and oxygen is modeled as a steady state, compressible, viscous and turbulent. Governing differential equations are solved using the CFD code provided by ANSYS Fluent.

2. LITERATURE SURVEY

Methane combustion has been the subject of many research areas including energy production for rocket propulsion. Both experimental and numerical studies are widely found in the literature [4]–[6]. In these studies, methane oxidation is modeled with the intermediate steps.

One of the oldest and most effective apparatus for obtaining laminar flames is Bunsen burner [7], [8]. Premixed combustion characteristics in Bunsen burner have been widely studied for years [9]–[13] for both turbulent and laminar flows. Bennett *et al.* [14] studied partially premixed flames including non-premixed combustion case.

Methane is also used as a preheater gas in hybrid rocket motors. Previously, Akyuzlu *et al.* [15]–[17] and Antoniou *et al.* [18] conducted several studies on combustion processes inside hybrid rocket motors. The authors aimed to develop a mathematical model in order to predict regression rate and to capture the physical mechanisms which contribute to the motor instabilities. These studies lead to the present study, that is, the study of combustion in methane – based low pressure rocket motors.

3. DESCRIPTION OF PHYSICAL MODEL

The Low Temperature Pressure Rocket Motor (LPRM) consists of oxygen plenum (FWD), combustion chamber (CC), mixing chamber (AFT) and a nozzle as presented in Figure 1.

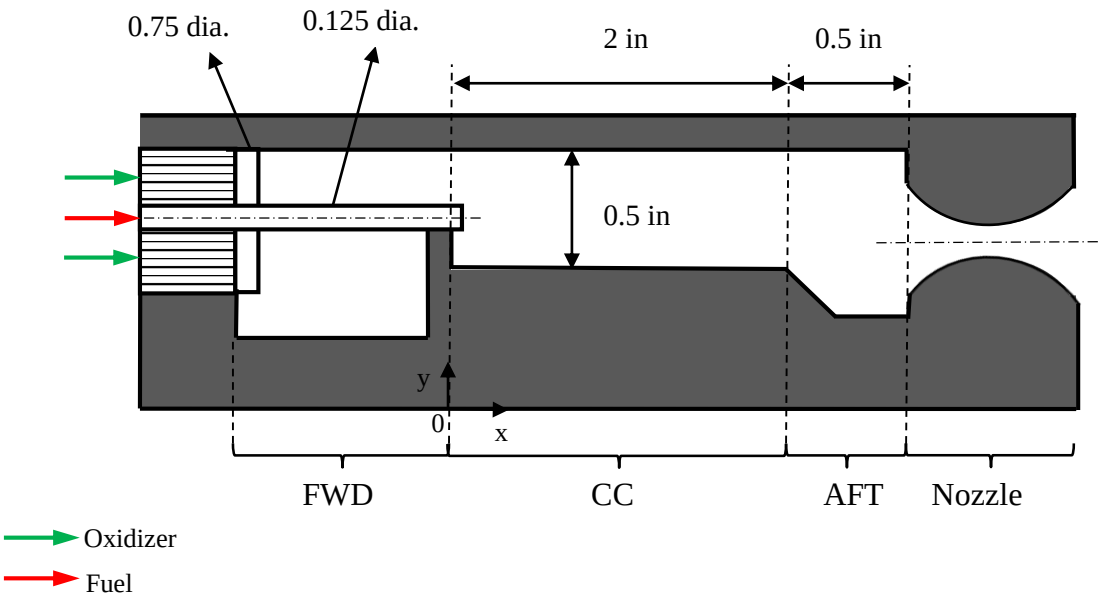

Figure 1. Physical model of the LPRM

Fuel (methane) enters to the system through 0.125 inch – diameter tube while oxidizer (oxygen) is supplied to the CC after straightened in FWD section. FWD section is not modeled in detail in the present study for simplicity. Cross sections of fuel and oxidizer tubes are first transformed to rectangular-shape by keeping inlet area same therefore flow variables, i.e. velocity and mass flow rate do not change. Width of the LPRM is 1.5 in. so aspect ratio is 3. Then the cross section of LPRM on x-y plane is considered as 2-D physical model of LPRM.

Reaction is initiated by ignition element at the outlet of fuel line. Assuming full combustion of fuel, oxygen and products flow through CC and exit from nozzle.

Following assumptions are made in order to develop the mathematical model:

1. The flow of oxygen and products are viscous, turbulent, subsonic, compressible and steady-state.
2. LPRM walls are adiabatic with an emissivity of 1.
3. Turbulent flow is formulated based on a two equation standard k-ε model.
4. Radiative heat transfer is modeled by P-1 Radiation model.

In order to simulate the reacting flow, the geometry of the combustion chamber of the LPRM is simplified. Several flow geometries are constructed to understand the characteristics of flow and reaction. First, a channel model (Ch) is developed as presented in Figure 2.

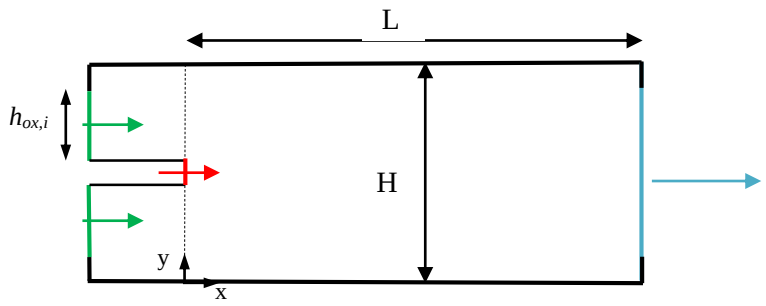

H = 0.5 in	height of LPRM
$h_{ox,i}$ = 2 x 0.125 in.	height of oxidizer inlet
$h_{f,i}$ = 0.01 in	height of fuel inlet
h_o = 0.375 in	height of outlet

Figure 2. Simplified geometry, Ch, for the present study

In geometry Ch, fuel is supplied at x = 0 and oxidizer feeds reaction. Reaction occurs around x = 0 and oxidizer and products leave combustion chamber at x = L = 2 in. In this simplified model, FWD is considered to be a 2-D, constant area channel and AFT and Nozzle are not included in this configuration.

The other simplified model, CCNF, is the most comprehensive model consisting FWD, CC, AFT and converging part of nozzle as presented in Figure 3.

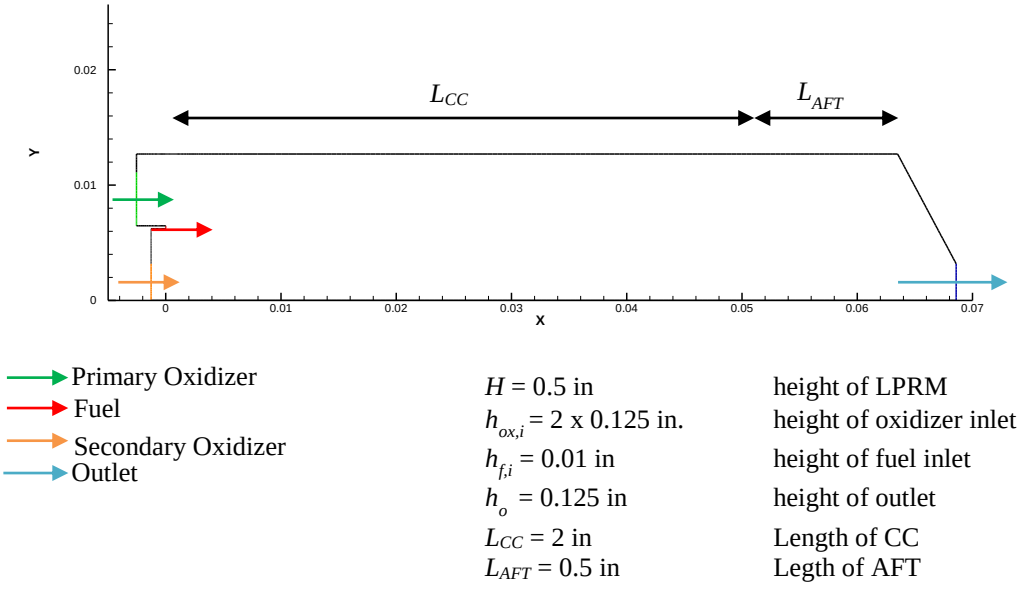

Figure 3. Schematic of simplified model, CCNF

The real LPRM geometry allows oxidizer flow at x < 0. Because of the transformation to two dimensional plane geometry, the fuel pipe acts as a restriction to oxidizer. Therefore, a secondary oxidizer inlet is added in order to simulate the 3-D effects at the combustion chamber inlet, although there is no secondary oxidizer inlet in the actual LPRM.

4. EXPERIMENTAL STUDY

4.1. Description of the Experimental Setup

The experimental test setup consists of methane (CH_4), gaseous oxygen (GO_2) and gaseous nitrogen (GN_2) supply tanks, the test stand, a series of pipes, fittings and valves, pressure gauges, pressure and differential pressure transducers, thermocouples, the LPRM and Data Acquisition (DAQ) system. Test setup is presented in Figure 4 and Figure 5.

Figure 4. LPRM Test Stand, Gas Supplies and DAQ System

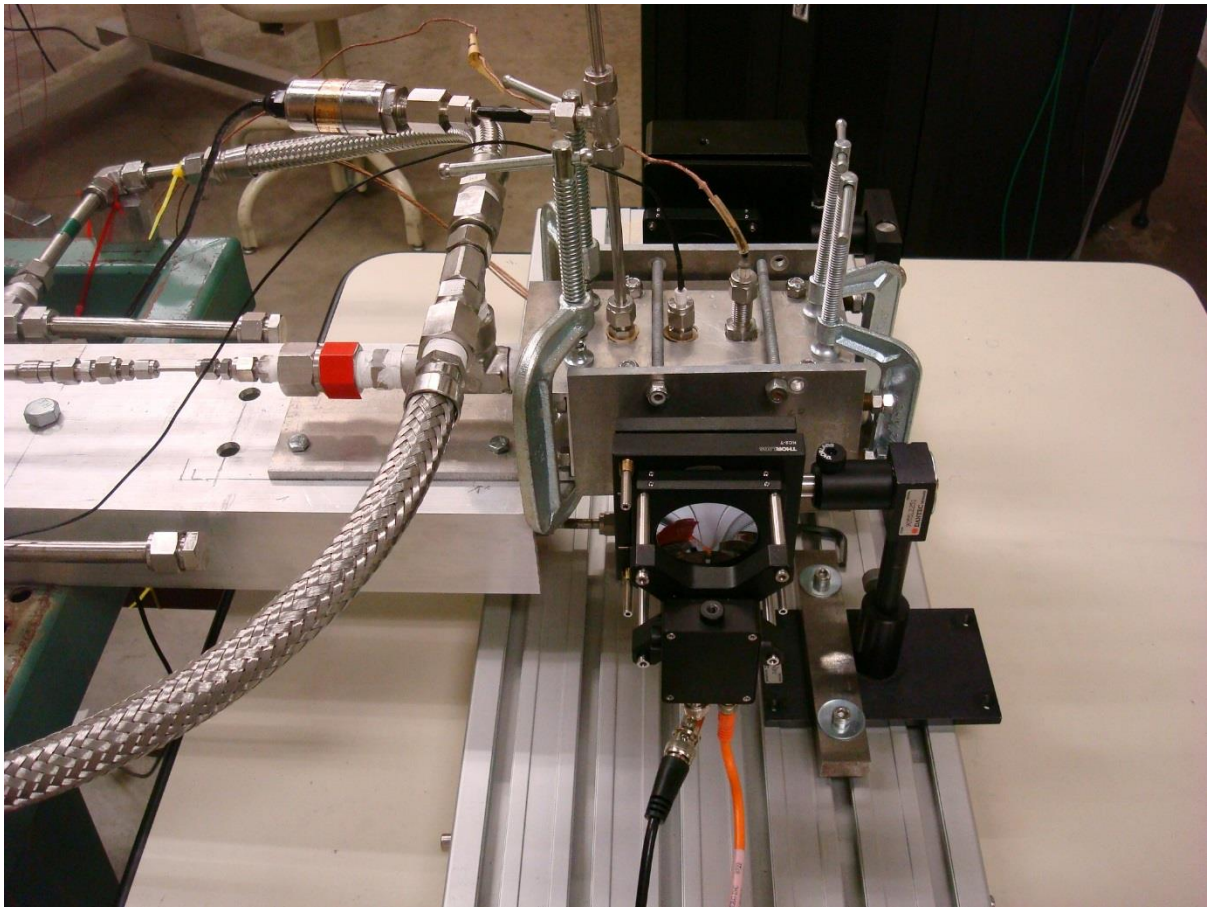

Figure 5. Low-Pressure Rocket Motor (LPRM)

Methane and oxygen are supplied from the pressurized supply tanks by regulating the flow with control valves. Methane flows through the middle pipeline and temperatures and pressures are measured by thermocouples and pressure transducers respectively and recorded by DAQ system. Flow rates of methane and oxygen are adjusted using needle valves located at the upstream of the LPRM.

LPRM consists of an oxygen plenum (FWD), combustion chamber (CC), a mixing chamber (AFT) and a nozzle (N). Methane enters LPRM through CC and oxygen enters FWD sections. Combustion takes place downstream of methane line in the CC, where ignition is accomplished by electric igniter. Combustion products and oxidizer exits LPRM through the nozzle. Gaseous nitrogen is used for purging.

LPRM is made of alumina silicate ceramic because of its high corrosion resistance and low thermal expansion. Stainless steel sheets are used in order to secure mechanical stability and reduce vibration. LPRM consists of one pressure transducer and four K-type thermocouples (three for the flame and one for the chamber). In Figure 6, inside of LPRM (top view) is presented indicating different sections of motor and thermocouples.

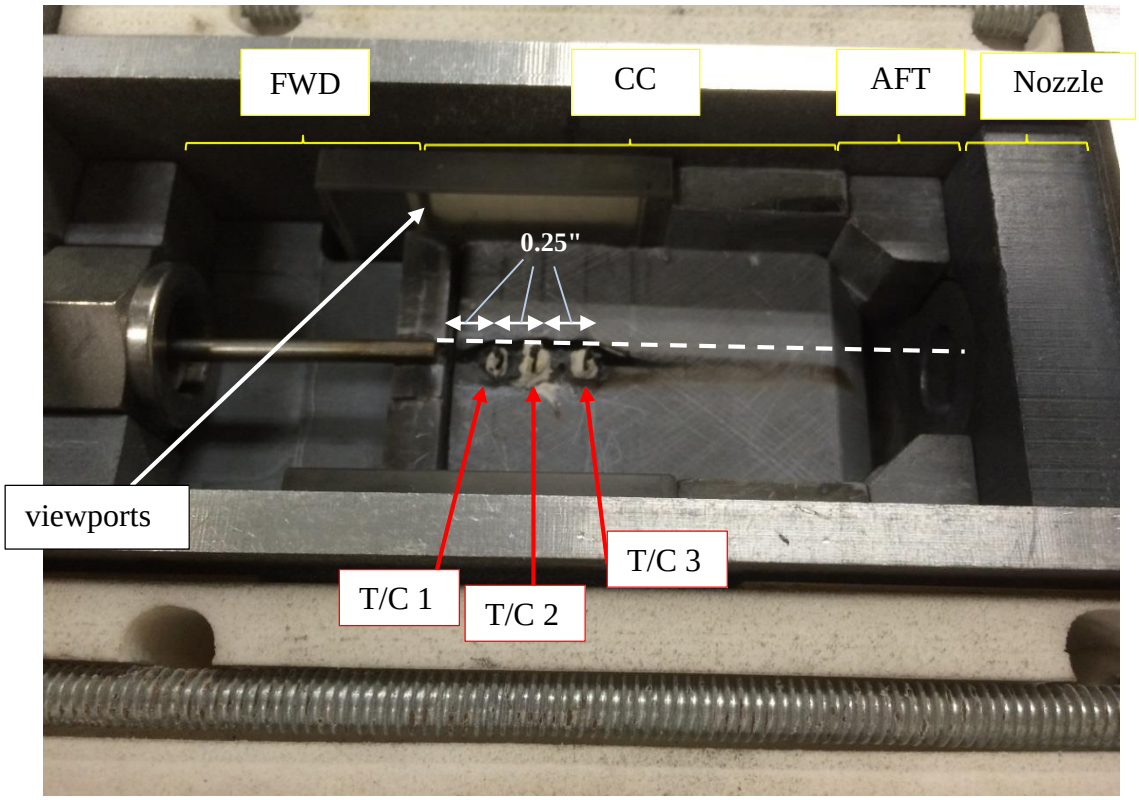

Figure 6. Inside view of LPRM and locations of thermocouples

Quarter inch quartz viewports are located at the both side of the LPRM to observe the flame.

Piping and instrumentation diagram of the test setup is presented in Figure 7. Instruments used in the experiments are listed in Appendix I.

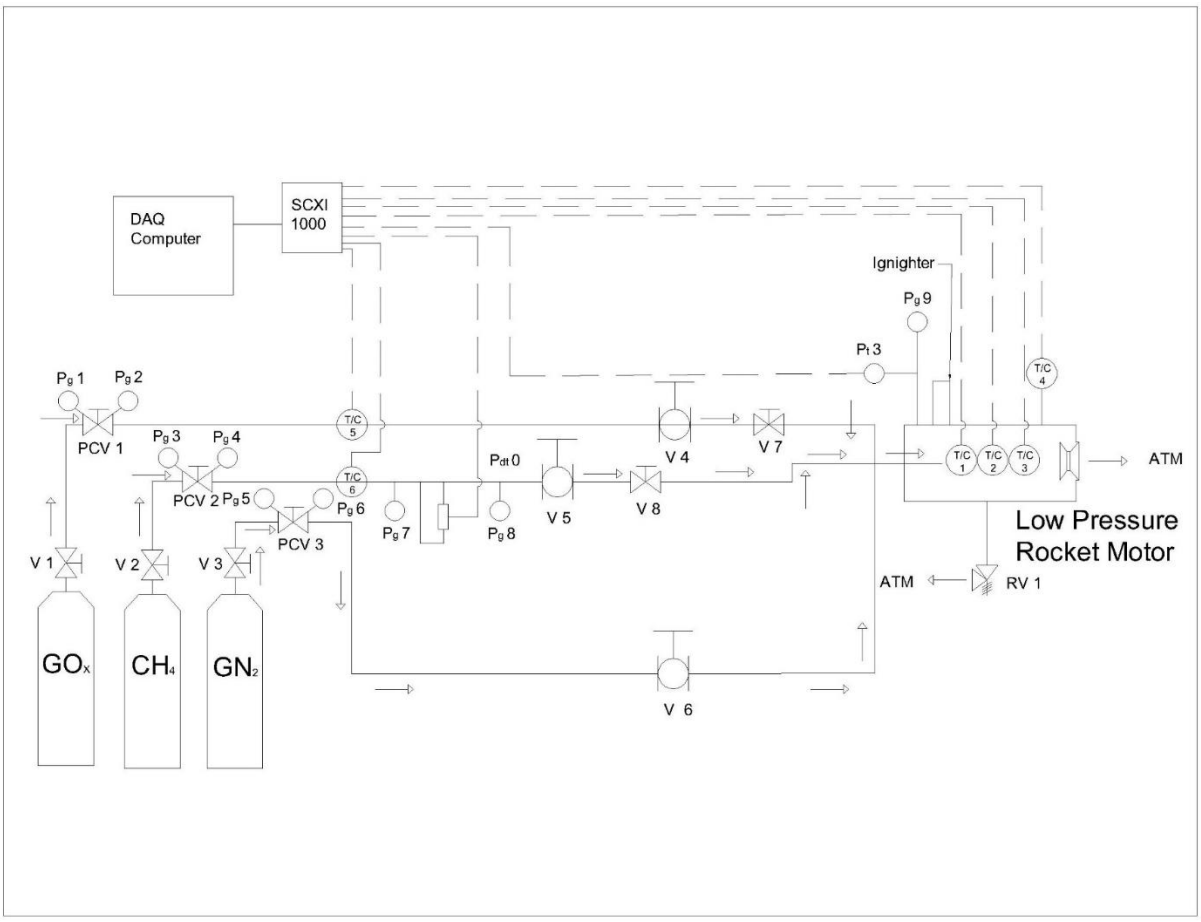

Figure 7.Piping (and Instrumentation) diagram of the test setup

4.2. Experimental Procedure and Operating Conditions

Before starting the experiment, the pressure transducers at the methane inlet and combustion chamber are calibrated. Calibration curves are presented in Appendix II. Experimental procedure is listed below:

1. Thermocouples, pressure and differential pressure transducers and DAQ system are checked and calibrated. LPRM is purged with gaseous nitrogen.
2. Methane tank pressure is set to the operating pressure value.
3. DAQ system is started.
4. Methane and oxygen are injected to LPRM by adjusting their flow rate values to operating conditions by the needle valves separately.

5. Methane is ignited by the electric igniter. If methane is not ignited, LPRM is purged with nitrogen.
6. After a course of time (see operating conditions), needle valves are shut down and the system is cooled down.
7. DAQ is stopped and the system is purged.

4.3. Data Analysis

Mass flow rate of methane is calculated using the change of pressure measured by the differential pressure transducer. These calculations are based on Equations presented in Appendix III.

5. NUMERICAL STUDY

In this chapter, the mathematical model of the LPRM which is used in the numerical simulations is presented. Governing differential equations and boundary conditions for the proposed mathematical model are presented in Section 5.1 based on the assumptions listed in Chapter 3. Solution technique is discussed in Section 5.2. ANSYS Fluent is used as a solver.

5.1. Mathematical Formulation

The governing differential equations for viscous, turbulent, compressible, unsteady flow of a Newtonian fluid in 2–D planar Cartesian coordinates are presented below. Vector form of the equations are presented in Appendix IV.

Continuity equation is given by:

$$\frac{\partial \rho}{\partial t} + \frac{\partial}{\partial x}(\rho u) + \frac{\partial}{\partial y}(\rho v) = 0 \tag{1}$$

The momentum equation in the x- and y-direction become:

$$\frac{\partial}{\partial t}(\rho u) + \frac{\partial}{\partial x}(\rho u u) + \frac{\partial}{\partial y}(\rho u v) + \frac{\partial p}{\partial x} - \frac{\partial}{\partial x}\left[\mu_{eff}\left(2\frac{\partial u}{\partial x} - \frac{2}{3}\vec{\nabla}\cdot\vec{V}\right)\right] - \frac{\partial}{\partial y}\left[\mu_{eff}\left(\frac{\partial u}{\partial y} + \frac{\partial v}{\partial x}\right)\right] = 0 \tag{2}$$

$$\frac{\partial}{\partial t}(\rho v) + \frac{\partial}{\partial x}(\rho v u) + \frac{\partial}{\partial y}(\rho v v) + \frac{\partial p}{\partial y} - \frac{\partial}{\partial x}\left[\mu_{eff}\left(\frac{\partial v}{\partial x} + \frac{\partial u}{\partial y}\right)\right] - \frac{\partial}{\partial y}\left[\mu_{eff}\left(2\frac{\partial v}{\partial y} - \frac{2}{3}\vec{\nabla}\cdot\vec{V}\right)\right] = 0 \tag{3}$$

respectively.

where μ_{eff} is the effective viscosity and defined as $\mu_{eff} = \mu + \mu_t$ and μ_t is the eddy viscosity which can be found using Standard k – ε model as:

$$\mu_t = \rho C_\mu \frac{k^2}{\varepsilon} \tag{4}$$

where k and ε are turbulence kinetic energy and turbulence dissipation rate respectively and C_μ is a constant. Transport equations for the Standard k – ε model are given as:

$$\frac{\partial}{\partial t}(\rho k) + \frac{\partial}{\partial x}(\rho u k) + \frac{\partial}{\partial y}(\rho v k) - \frac{\partial}{\partial x}\left(\left(\mu + \frac{\mu_t}{Pr_k}\right)\frac{\partial k}{\partial x}\right) - \frac{\partial}{\partial y}\left(\left(\mu + \frac{\mu_t}{Pr_k}\right)\frac{\partial k}{\partial y}\right) - \mu_t S^2 + \rho\varepsilon = 0 \tag{5}$$

$$\frac{\partial}{\partial t}(\rho \varepsilon) + \frac{\partial}{\partial x}(\rho u \varepsilon) + \frac{\partial}{\partial y}(\rho v \varepsilon) - \frac{\partial}{\partial x}\left(\left(\mu + \frac{\mu_t}{Pr_\varepsilon}\right)\frac{\partial \varepsilon}{\partial x}\right) - \frac{\partial}{\partial y}\left(\left(\mu + \frac{\mu_t}{Pr_\varepsilon}\right)\frac{\partial \varepsilon}{\partial y}\right) - C_{\varepsilon 1}\frac{\varepsilon}{k}\mu_t S^2 + \rho C_{\varepsilon 2}\frac{\varepsilon^2}{k} = 0 \tag{6}$$

where Pr_k and Pr_ε are turbulent Prandtl numbers for k and ε, $C_{\varepsilon 1}$ and $C_{\varepsilon 2}$ are constants respectively. For this model, constants have the following values [19]:

$Pr_k = 1.0$, $Pr_\varepsilon = 1.3$, $C_{\varepsilon 1} = 1.44$ and $C_{\varepsilon 2} = 1.92$

S is the modulus of the mean rate of strain tensor, which is defined as:

$$S = \sqrt{2 S_{ij} S_{ij}}$$

The energy equation is given by:

$$\frac{\partial}{\partial t}(\rho c_p T) + \frac{\partial}{\partial x}(\rho c_p u T) + \frac{\partial}{\partial y}(\rho c_p v T) - \frac{\partial}{\partial x}\left(k_{eff}\frac{\partial T}{\partial x}\right) - \frac{\partial}{\partial y}\left(k_{eff}\frac{\partial T}{\partial y}\right) - \Phi + \dot{Q}_r - \dot{Q}_{gen} + D_j = 0 \tag{7}$$

where

c_p is the specific heat of the mixture which is found as: $c_p = \sum_i Y_i c_{p,i}$ and specific heats of individual species are calculated using 4th order polynomials [20].

k_{eff} is the effective thermal conductivity and defined as: $k_{eff} = k + \frac{c_p \mu_t}{Pr_t}$

Φ is the viscous dissipation term

$\dot{Q}_r$ is the radiative heat transfer which is found using P-1 Radiation model ([21], [22]) as:

$$\dot{Q}_r = aG - 4an^2\sigma T^4 \tag{8}$$

where G is the incident radiation and can be found from the following equation:

$$\nabla \cdot \left(\frac{1}{3(a+\sigma_s) - C\sigma_s} \nabla G \right) - aG + 4an^2\sigma T^4 = 0 \tag{9}$$

where a is the absorption coefficient, n is the refractive index of the medium and σ is Stefan-Boltzmann constant.

$\dot{Q}_{gen}$ is the source of energy due to chemical reaction which is defined as:

$$\dot{Q}_{gen} = -\sum_j \frac{H_j}{M_j} R_j \tag{10}$$

where H_j is the enthalpy of formation of species j and R_j is the rate of creation of species j.

D_j is equal to $D_j = \sum_j h_j J_j$ which represents the energy transfer due to species diffusion where J_j is the diffusion flux of species j which is defined for turbulent flows as:

$$J_i = -\left(\rho D_{i,m} + \frac{\mu_t}{Sc} \right) \nabla Y_i - D_{T,i} \frac{\nabla T}{T} \tag{11}$$

where $D_{m,i}$ and $D_{T,i}$ are mass and thermal diffusion coefficients respectively and Sc is the Schmidt number which is defined as $Sc = \frac{\mu_t}{\rho D_t}$.

And transport of species is modeled as

$$\frac{\partial(\rho Y_i)}{\partial t} + \frac{\partial(\rho u Y_i)}{\partial x} + \frac{\partial(\rho v Y_i)}{\partial y} - \frac{\partial}{\partial x}\left(\left(\rho D_{m,i} + \frac{\mu_t}{Sc}\right)\frac{\partial Y_i}{\partial x} + D_{T,i}\frac{1}{T}\frac{\partial T}{\partial x}\right) - \frac{\partial}{\partial y}\left(\left(\rho D_{m,i} + \frac{\mu_t}{Sc}\right)\frac{\partial Y_i}{\partial y} + D_{T,i}\frac{\partial T}{\partial y}\right) - R_i = 0 \quad (12)$$

where Y_i is the mass fraction of i^{th} species. R_i is the net rate of production of species i by chemical reaction. There are several models to describe rate of production. In this study, Laminar Finite Rate Model (LFRM) and Eddy-Dissipation Model (EDM) are compared and a solution procedure is suggested which utilizes both reaction models.

LFRM computes the species source terms using Arrhenius chemical kinetics. The net source of species i due to reaction is calculated as:

$$R_i = M_i\left(\nu_i^p - \nu_i^r\right)\left(k_f \prod_{j=1}^{N}\left[C_j\right]^{\eta_j}\right) \quad (13)$$

where

M_i is the molecular mass of species i

ν_i^r and ν_i^p are the stoichiometric coefficients for reactant and product respectively,

k_f is the Arrhenius reaction rate and defined as:

$k_f = A_r e^{-E_r/RT}$ where A_r is the pre-exponential factor, E_r is the activation energy for the reaction and R is the universal gas constant and

C_j is the molar concentration of each reactant and product species j.

EDM calculates R_i by taking the minimum value of the following two expressions:

$$R_{i,r} = \nu_i^r M_i A \rho \frac{\varepsilon}{k} min_R \left[\frac{Y_R}{\nu_{i,R}^r M_R} \right]$$
$$R_{i,r} = \nu_i^r M_i AB \rho \frac{\varepsilon}{k} \frac{\sum_P Y_P}{\sum_j^N \nu_j^p M_j} \quad (14)$$

where A and B are empirical constants and equal to 4.0 and 0.5 respectively.

Combustion of methane takes place according to single reaction four species assumption:

$$CH_4 + 2O_2 \rightarrow CO_2 + 2H_2O$$

Then the production rate of fuel, methane becomes:

$R_f = M_f \left(k_f C_f^{0.2} C_{ox}^{1.3} \right)$ using LFRM. The reaction rate by EDM changes according to Equation 14.

Boundary conditions for the GDE are provided to Fluent solver as follows: Mass flow rate of fuel and oxidizer are given at inlets. Prescribed oxidizer mass flow rate is determined to provide a stoichiometric value for oxidizer to fuel mass ratio. Additionally, temperatures are prescribed at inlets. Mass fraction of methane at fuel inlet is defined as 1.0 and mass fraction of oxygen at oxidizer inlet(s) are defined as 0.7 except for Bunsen burner simulations. In Bunsen burner simulations, air (Y_{O2} = 0.23) is taken as oxidizer. At outlet, pressure is given as the boundary condition. LPRM walls are modeled as adiabatic. All the walls and inlet and outlet are considered as radiative surfaces with an emissivity of 1.0.

5.2. Solution Technique

The governing equations are solved in 2-D planar space by pressure based solver provided by ANSYS Fluent. Coupled scheme is used for pressure-velocity coupling and spatial discretization is done based on second – order upwind scheme.

In order to simulate viscous, turbulent, compressible, unsteady reacting flow of a Newtonian fluid, the following models by ANSYS Fluent are used: Energy, Turbulence – Standard k-epsilon, Radiation – P1, Species – Species Transport.

False (Pseudo)-transient under-relaxation method is also used for more robust solutions.

Summary of the solver and calculation settings and solution methods are presented in Table 1.

Table 1. Solver settings, solution methods and calculation methods for the present study

Solver Settings	
	Pressure – based
	2 – D Planar
	Steady
Solution Methods	
	Scheme – Coupled
	Gradient – Least Squares Cell Based
	Pressure – 2^{nd} Order
	Discretization – 2^{nd} Order Upwind
	Pseudo – Transient
Calculation Settings	
	Residual Criteria: 10^{-15} for Non-Reacting
	10^{-9} for Reacting

For the numerical simulations of steady-state reacting flows, modeling ignition is very difficult because the nature of chemical reactions is unsteady. ANSYS Fluent provides Patching option which imposes certain conditions to specific locations in the domain. These

imposed conditions are utilized as the initial guess of the iterative calculations. Ignition is simulated by imposing high temperature (~1750 K) on a specified region close to fuel inlet (x = 0 – 0.15 in, y = 0.245 – 0.255 in) as the initial guess. Convergence is another problematic aspect of the reacting flow simulations. For this purpose, a solution procedure is utilized which requires an iterative reduction of the assumed value of the fuel inlet temperature by the user.

1. Initialize the simulation for non-reacting cold flow of fuel and oxidizer. Run until convergence is attained.
2. Once Step 1 is complete, update fuel inlet boundary condition: Tfi = 1500 K. Run until solution converges.
3. Turn on Reaction – LFRM, patch 1750 K to fuel inlet. Run until solution converges.
4. Update boundary condition for fuel inlet: Tfi = 1200 K. Patch 1750 K to the same region. Run until convergence is achieved.
5. Repeat Step 4 for Tfi = 900, 600, 300 K.
6. Once a converged solution is obtained at Step 5, turn reaction model to EDM without initializing or patching and run until solution converges.

6. RESULTS

In this chapter, results of the experiments and the computational simulations are presented. Results include the experiment results, simulation of benchmark cases, grid independence study as well as comparison of the experimental and computational study and finally the results of the parametric study.

6.1. Results of the Experiments

In the present study, the operating conditions in Table 2 are used for hot test runs.

Table 2. Operating conditions for the experiments

	Gas	Supply Tank Regulator Setting	Needle valve Ignition Setting	Needle valve Steady State Setting	
Fuel	Methane	40 psig	10°	10°	5°
Oxidizer	Oxygen	40 psig	20°	20°	10°
Purge	Nitrogen	40 psig	0°	0°	0°

Additionally, the experimental matrix is presented in Table 3.

Table 3. Experimental matrix

Chamber Pressure	Chamber Temperature	Flame Temperatures 1, 2,3	Mass Flow Rate of Fuel
M	M	M	C

M: measured, C: empirically calculated

Two different runs are conducted with the same operating conditions. In this section, results of the Run 1 are presented. Results of Run 2 are presented in Appendix VI. In Table 4, results of Run 1 are tabulated and through Figure 8 to Figure 10, mass flow rate of methane, chamber pressure, temperature of gases inside chamber and temperature of flame at the locations specified in Figure 6 versus time are plotted, respectively.

Table 4. Chamber pressure, temperature, flame temperatures and mass flow rate of methane

Time (hh:mm:ss)	Chamber Pressure [psig]	Chamber Temperature [°C]	Flame Temperature T/C 1 [°C]	Flame Temperature T/C 2 [°C]	Flame Temperature T/C 3 [°C]	Mass flow rate of fuel [kg/s]
13:27:20	0.078	22.25	23.38	24.75	24.59	0
13:27:34	2.026	542.80	791.66	1090.40	1209.01	0.0001718
13:28:09	2.470	937.16	663.71	868.31	1066.80	0.0001487
13:28:51	0.886	478.33	713.26	1259.40	1364.75	0.0000701
13:29:05	0.074	285.41	592.18	635.59	578.80	0
13:30:00	0.076	68.07	291.61	195.63	188.24	0

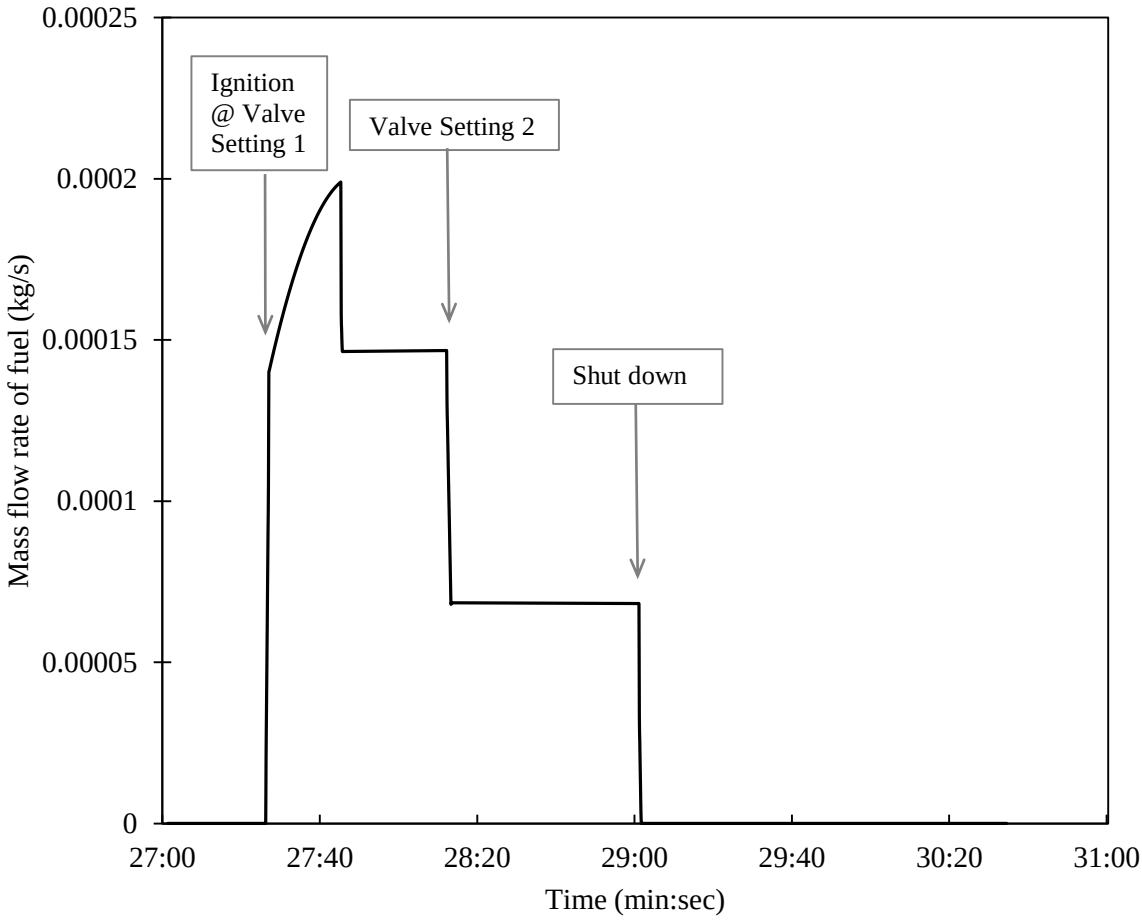

Figure 8. Mass flow rate of methane versus time for Run 1

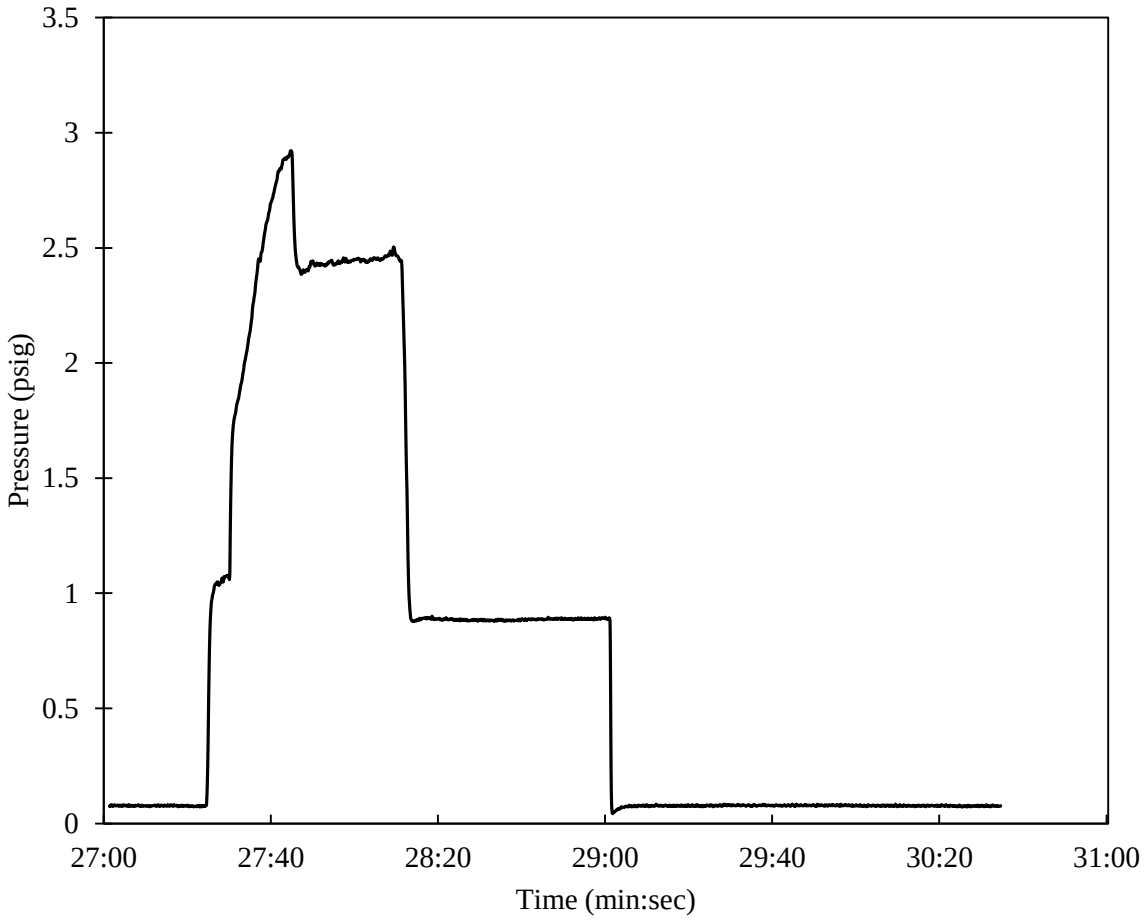

Figure 9. Recorded chamber pressure (Pt) for Run 1

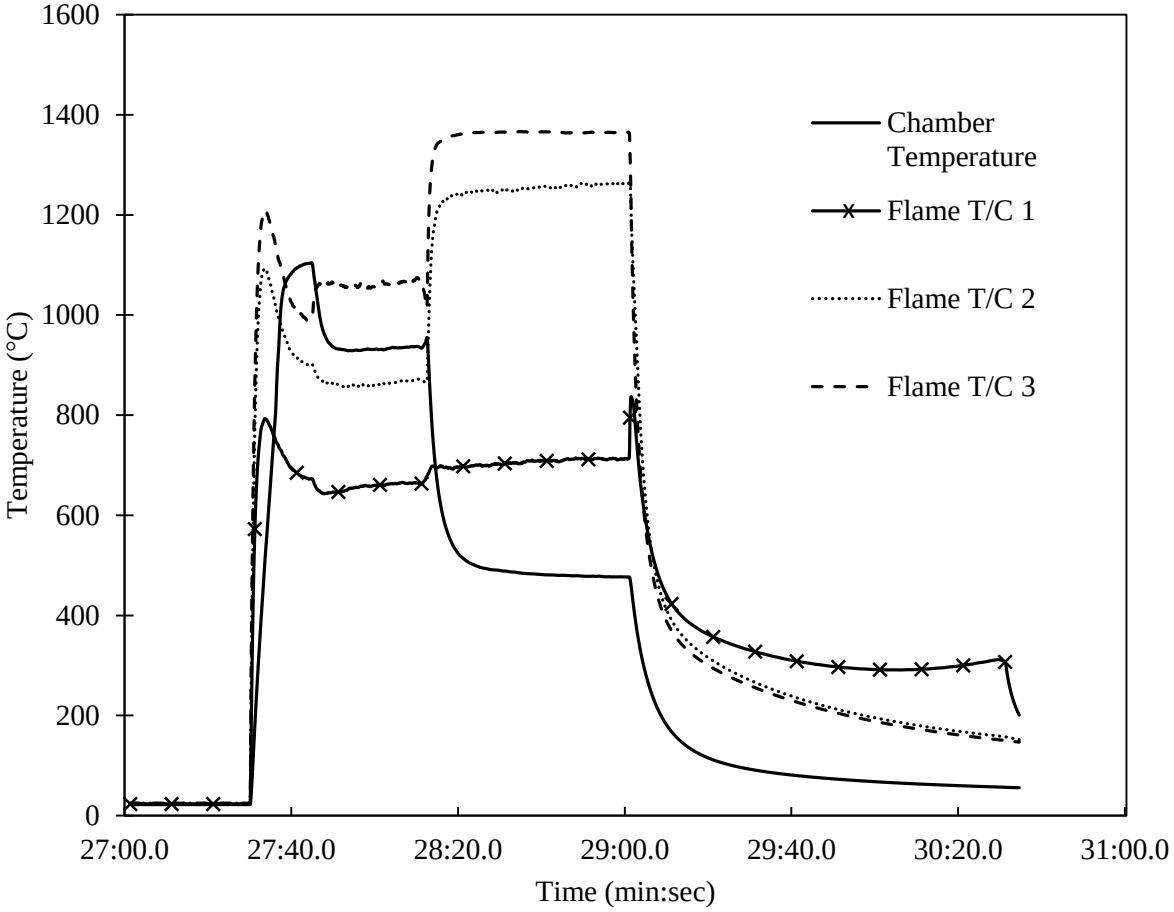

Figure 10. Registered temperatures (T/C) for Run 1

In addition to the experimental data presented above, pictures of the flame can be found in Figure 11 and Figure 12.

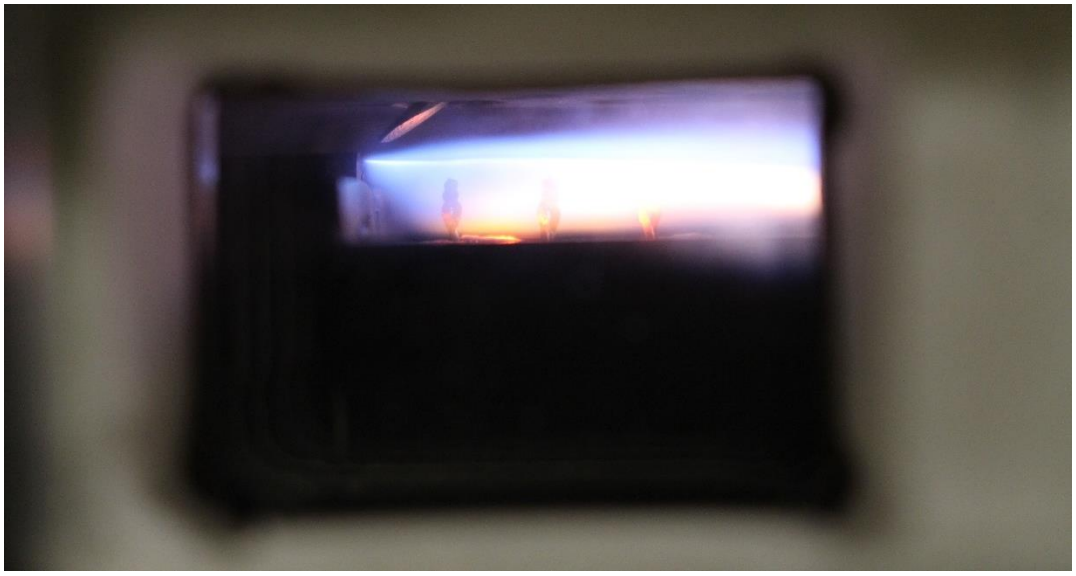

Figure 11. Picture of the flame from Run 1 at Valve Setting 1.

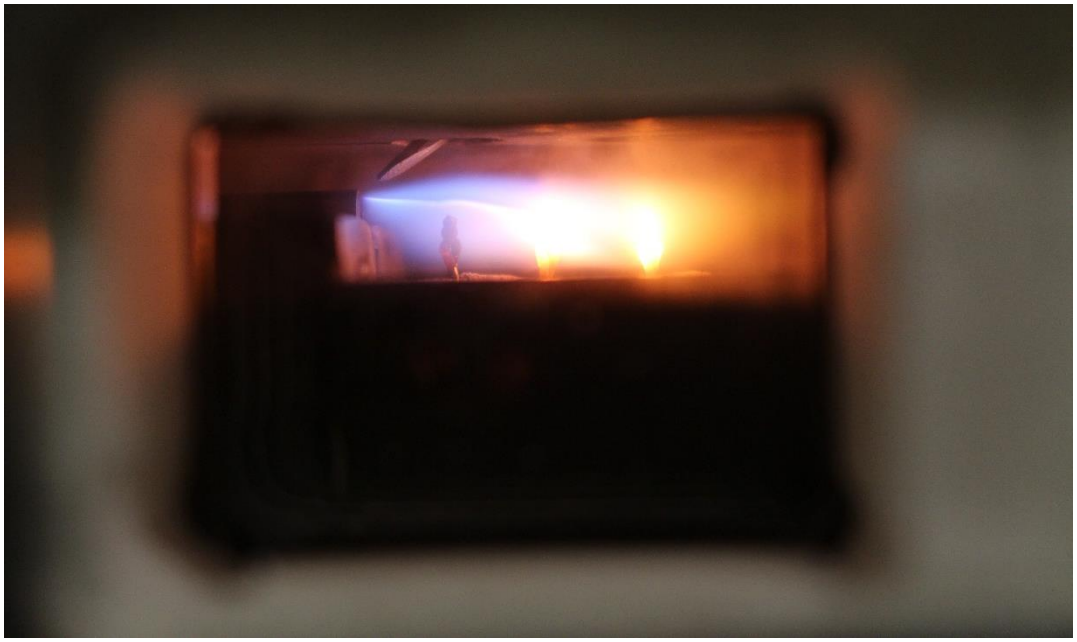

Figure 12. Picture of the flame from Run 1 at Valve Setting 2

6.2. Results of the Computational Model

In this section, results of the CFD simulations are presented. First, computational model is validated using Benchmark case studies. Validation is done based on non-reacting channel flow [23] and reacting flow in Bunsen burner. Additionally, simulations are verified to be independent of mesh size in Section 6.2.2. In the Section 6.3, computational and

experimental results are compared and following that results of the parametric study are introduced.

Operational parameters used in the computational studies are presented in Table 5.

Table 5. Operational Parameters in the simulations

Parameter	Symbol	Value	Unit
Inlet mass flow rates			
Fuel	$\dot{m}_f$	*	kg/s
Oxidizer	$\dot{m}_{ox}$	*	kg/s
Inlet Mass Fraction			
Fuel	$Y_{f,in}$	1.0	-
Oxidizer	$Y_{ox,in}$	*	-
Inlet Temperature	T_{in}	300	K
Outlet Pressure`	P_o	*	kPa

**Variable. See corresponding sections.*

6.2.1. Validation of Computational Model

6.2.1.1. Flow Characteristics

In order to validate the computational model, the study of Morihara *et al.* [23] is selected as a benchmark case. The authors presented the numerical solution to the flow in the entrance region of a semi-infinite parallel channel for various Reynolds numbers. Solutions for Re = 20, 200, and 2000 are considered as the benchmark case for the present study. A semi-infinite plate with a 0.05 m height is modeled and results are nondimensionalized in order to compare them.

In Table 6, the results of the present study and results of the benchmark case are tabulated. In Figure 13, these tabulated results are plotted.

Table 6. Non-dimensional centerline velocities of present study and Morihara et al.

Re	**20**			**200**			**2000**		
x'	**B.C.**	**P.S.**	**% Dev.**	**B.C.**	**P.S.**	**% Dev.**	**B.C.**	**P.S.**	**% Dev.**
0	1.00	1.00	0.00	1.00	1.00	0.00	1.00	1.00	0.00
0.005	1.01	1.006	-0.40	1.07	1.09	1.87	1.167	1.16	-0.60
0.01	1.03	1.022	-0.78	1.18	1.172	-0.68	1.23	1.233	0.24
0.015	1.05	1.048	-0.19	1.23	1.23	0.00	1.283	1.289	0.47
0.02	1.085	1.082	-0.28	1.28	1.276	-0.31	1.323	1.332	0.68
0.025	1.12	1.123	0.27	1.32	1.315	-0.38	1.361	1.367	0.44
0.03	1.18	1.165	-1.27	1.35	1.346	-0.30	1.389	1.394	0.36
0.035	1.22	1.208	-0.98	1.375	1.372	-0.22	1.414	1.415	0.07
0.04	1.26	1.249	-0.87	1.395	1.393	-0.14	1.431	1.431	0.00
0.06	1.37	1.376	0.44	1.45	1.447	-0.21	1.473	1.469	-0.27
0.08	1.44	1.443	0.21	1.47	1.471	0.07	1.485	1.484	-0.07

B.C.: Benchmark case of Morihara et al., P.S.: Present study

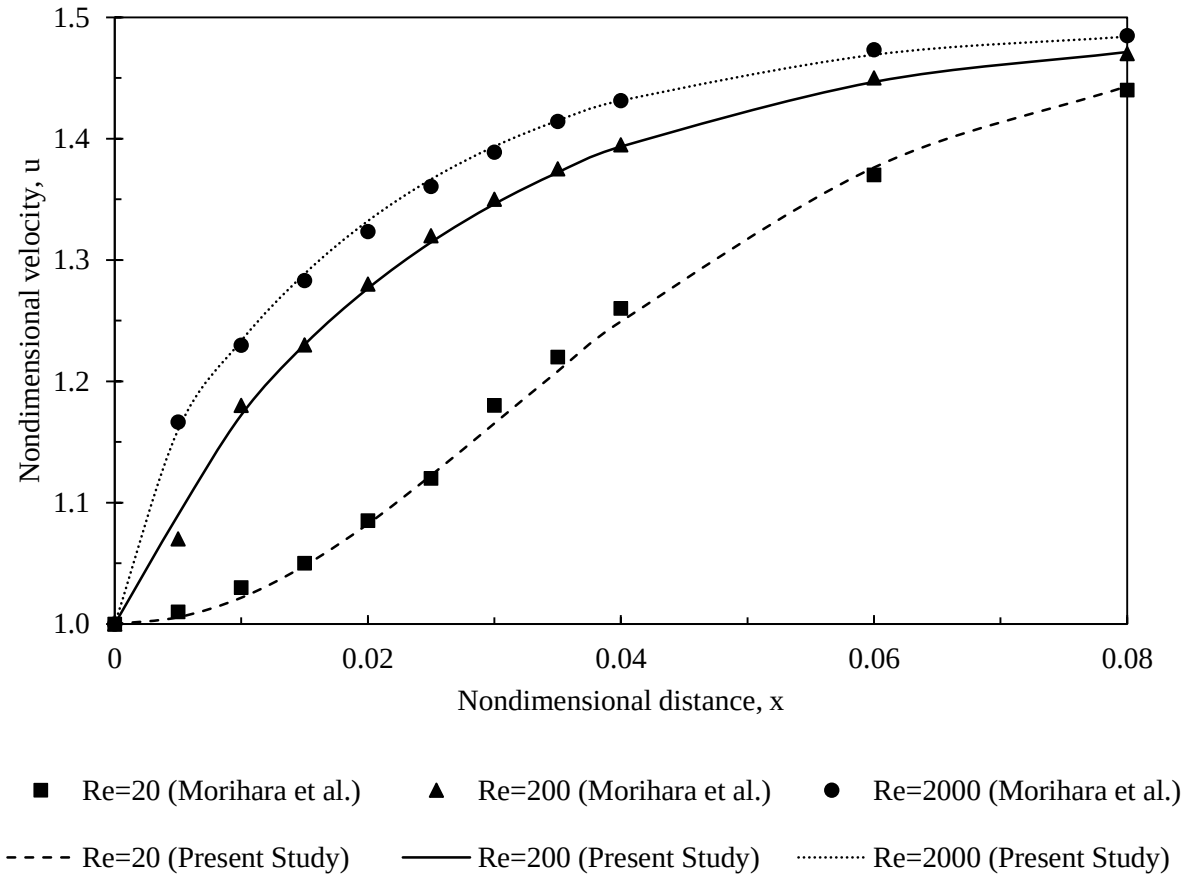

Figure 13. Comparison of non-dimensional centerline velocities predicted by the present study and by Morihara *et al*. for Re = 20,200, and 2000

6.2.1.2. Reacting Flow

Before carrying out the simulations of combustion inside LPRM model, flow in a Bunsen burner in Ch geometry is simulated. Results are obtained for three different oxidizer mass flow rates. Additionally, two different reaction models provided by ANSYS Fluent are utilized.

In Table 7, operating conditions and general results for the Run Ch-R-I are presented.

Table 7. Operating conditions and results for Run Ch-R-I

Run Number: Ch-R-I			RESULTS			
m_f	m_o	P_o	P_{in}	m_o	V_o	T_o
kg/s	kg/s	kPa	kPa	kg/s	m/s	K
0.0008	0.01	0	0.0018	0.01008	2.4	819
0.0008	0.02	0	0.0037	0.02008	3.4	624
0.0008	0.04	0	0.0085	0.04008	5.3	472

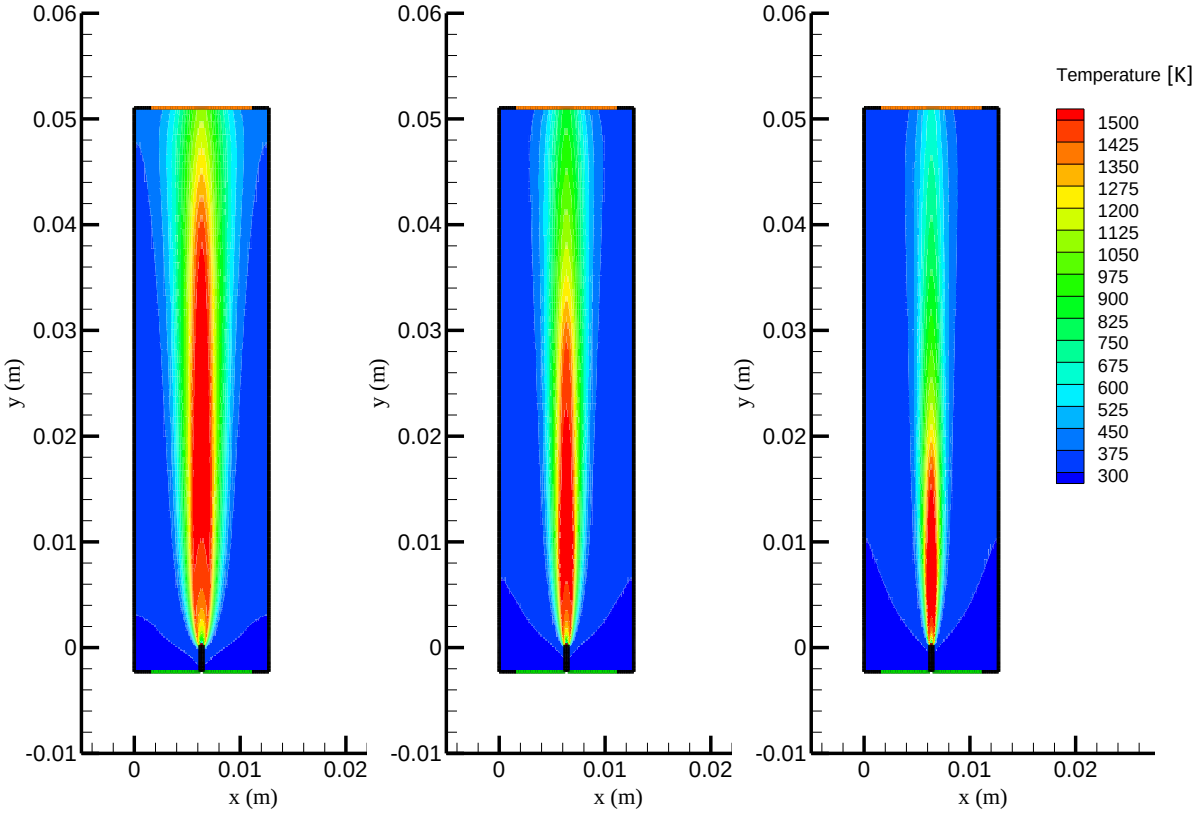

(a) (b) (c)

Figure 14. Temperature distribution (in Kelvins) for Bunsen burner inside Channel simulation with Eddy – Dissipation Reaction model for different mass flow rates of oxidizer: (a) $\dot{m}_{ox}$ = 0.01 kg/s, (b) $\dot{m}_{ox}$ = 0.02 kg/s, $\dot{m}_{ox}$ = 0.04 kg/s

Bunsen burner is also modeled with LFRM without employing Step 5 of the solution procedure. As can be seen in Figure 15, LFRM over-estimates the flame temperature.

Therefore, for the other reacting flow simulations, all the steps of solution procedure, which involve ED reaction model, are followed exactly.

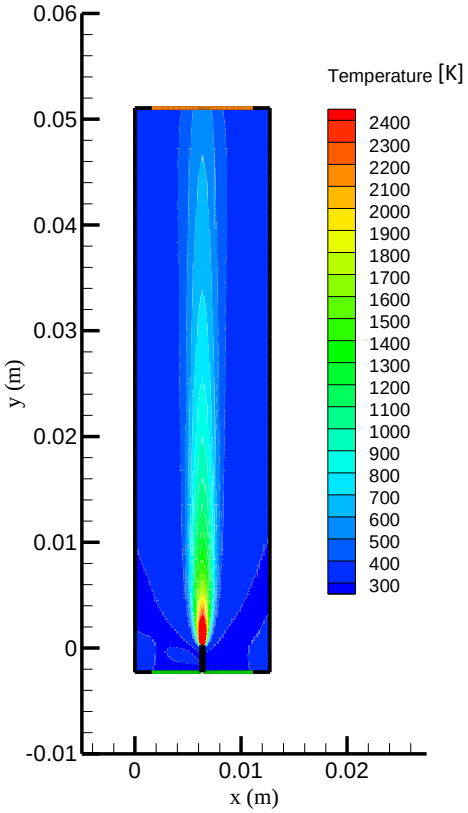

Figure 15. Temperature distribution (in Kelvins) inside Channel for Bunsen Burner simulation with Laminar Finite Rate Reaction model

6.2.2. Grid Independence Study

Grid (mesh) independence study is conducted for non-reacting and reacting flows separately. Only Channel (Ch) model is taken into consideration because the other geometries are generated based on Channel.

Four different grids are constructed for this study. All of them are stretched in y – direction and three of them are also stretched in x – direction. Stretching is geometric with a growth rate 1.1. Characteristics of these grids are summarized in Table 8. These grids are presented in Figure 16 and Figure 17.

Table 8. Properties of different meshes

Mesh	Number of Cells along x and y direction	Stretching
1	105 x 72	Only y - direction
2	140 x 80	x and y direction
3	150 x 88	x and y direction
4	160 x 94	x and y direction

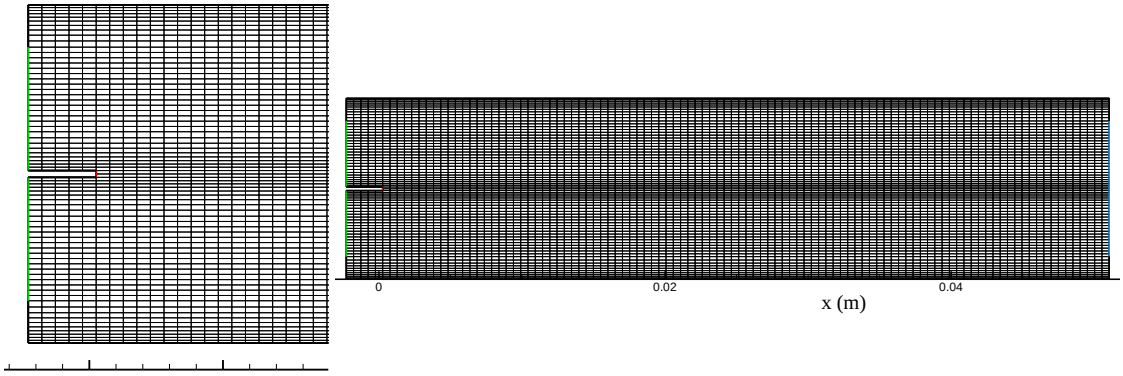

Figure 16. Mesh 1

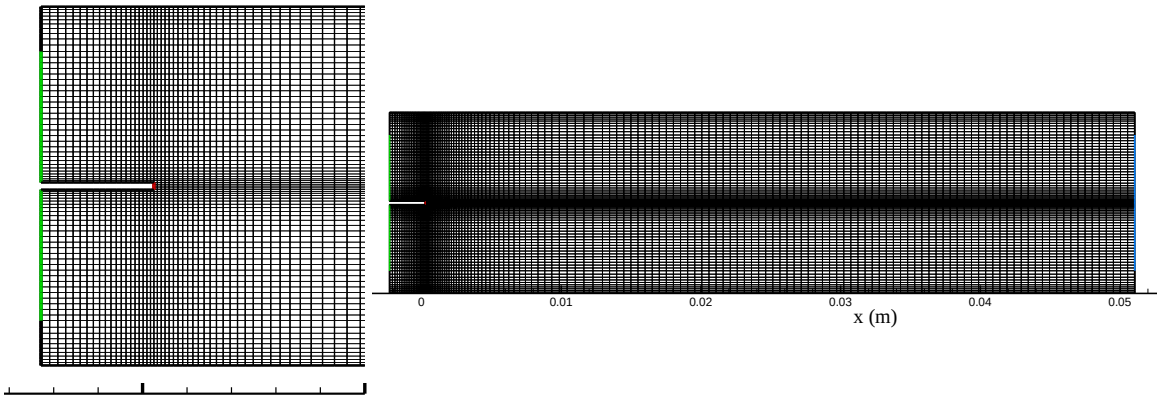

Figure 17. Mesh 2, 3 and 4

6.2.2.1. Non-Reacting Flow

In order to check that accuracy of the predictions and convergence of solutions are independent of the selected grid size, simulations of non-reacting flows are considered. For this purpose, mixing flow of methane and oxygen is simulated inside the Channel configuration. Results are compared based on velocity and methane mass fraction profiles along centerline and along a vertical line near the fuel inlet.

Table 9. Operating parameters and results for Run Ch-NR-I

Run Number: Ch-NR-I				RESULTS		
Mesh	m_f	m_o	P_o	P_{in}	m_o	V_o
	kg/s	kg/s	kPa	kPa	kg/s	m/s
Mesh 1	0.00066	0.01056	0	0	0.01122	1.02
Mesh 2	0.00066	0.01056	0	0	0.01122	1.04
Mesh 3	0.00066	0.01056	0	0	0.01122	1.08
Mesh 4	0.00066	0.01056	0	0	0.01122	1.07

Axial velocity distribution along centerline is tabulated in Table 10 and plotted in Figure 18.

Table 10. Axial velocity along centerline using different meshes

x [m]	Velocity [m/s]			
	Mesh 1	Mesh 2	Mesh 3	Mesh 4
0.000	3.689	3.868	4.010	4.022
0.005	1.597	1.667	1.735	1.744
0.010	1.389	1.436	1.475	1.480
0.015	1.294	1.329	1.356	1.359
0.020	1.231	1.261	1.281	1.284
0.025	1.182	1.208	1.225	1.227
0.030	1.138	1.162	1.177	1.179
0.036	1.100	1.121	1.134	1.135
0.041	1.068	1.086	1.097	1.098
0.046	1.059	1.073	1.083	1.083
0.051	1.181	1.189	1.192	1.193

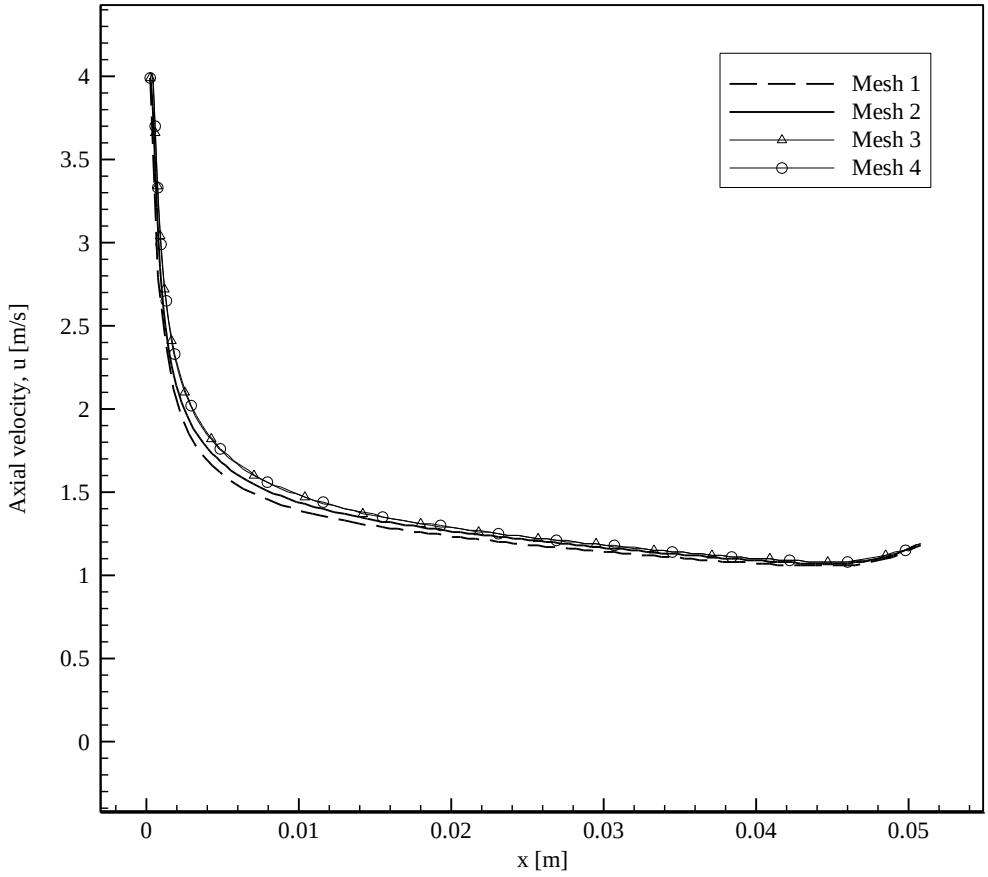

Figure 18. Axial velocity along centerline of Ch using different meshes

Mass fraction of methane along centerline is tabulated in Table 11 and plotted in Figure 19.

Table 11. Mass fraction of methane along centerline using different meshes

x [m]	Mass fraction of methane []			
	Mesh 1	Mesh 2	Mesh 3	Mesh 4
0.000	1.0000	1.0000	1.0000	1.0000
0.005	0.2256	0.2389	0.2567	0.2587
0.010	0.1643	0.1728	0.1825	0.1835
0.015	0.1354	0.1416	0.1480	0.1486
0.020	0.1168	0.1217	0.1264	0.1269
0.025	0.1032	0.1073	0.1109	0.1113
0.030	0.0928	0.0962	0.0990	0.0993
0.036	0.0847	0.0874	0.0897	0.0899
0.040	0.0783	0.0804	0.0822	0.0824
0.046	0.0734	0.0750	0.0763	0.0764
0.051	0.0693	0.0704	0.0714	0.0715

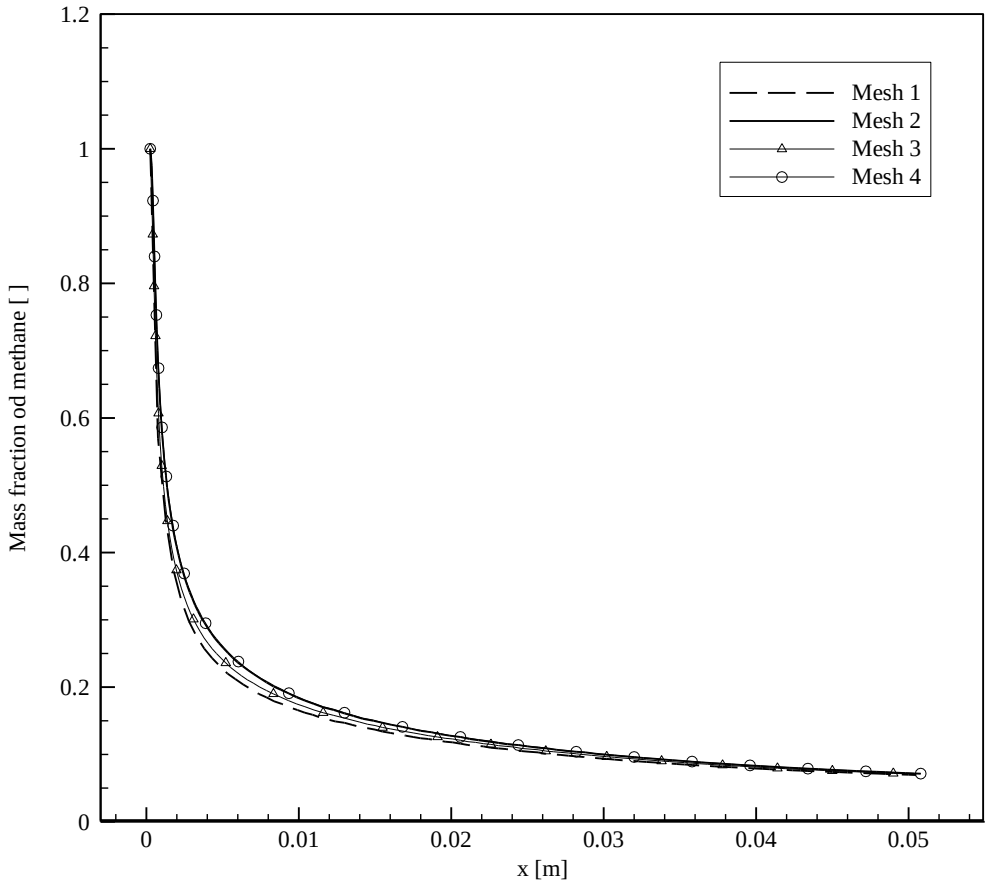

Figure 19. Mass fraction of methane along centerline using different meshes

In addition to centerline, a vertical line near fuel inlet (x = 0.00127) is also taken into account. Axial velocity distribution is tabulated in Table 12 and plotted in Figure 20.

Table 12. Axial velocity along vertical axis at x = 0.00127 m

y [m]	Axial velocity [m/s]			
	Mesh 1	Mesh 2	Mesh 3	Mesh 4
0.000	0.000	0.000	0.000	0.000
0.001	0.382	0.369	0.370	0.369
0.003	0.781	0.801	0.805	0.806
0.005	0.874	0.867	0.870	0.871
0.008	0.874	0.867	0.870	0.871
0.010	0.781	0.801	0.805	0.806
0.011	0.382	0.369	0.370	0.369
0.013	0.000	0.000	0.000	0.000

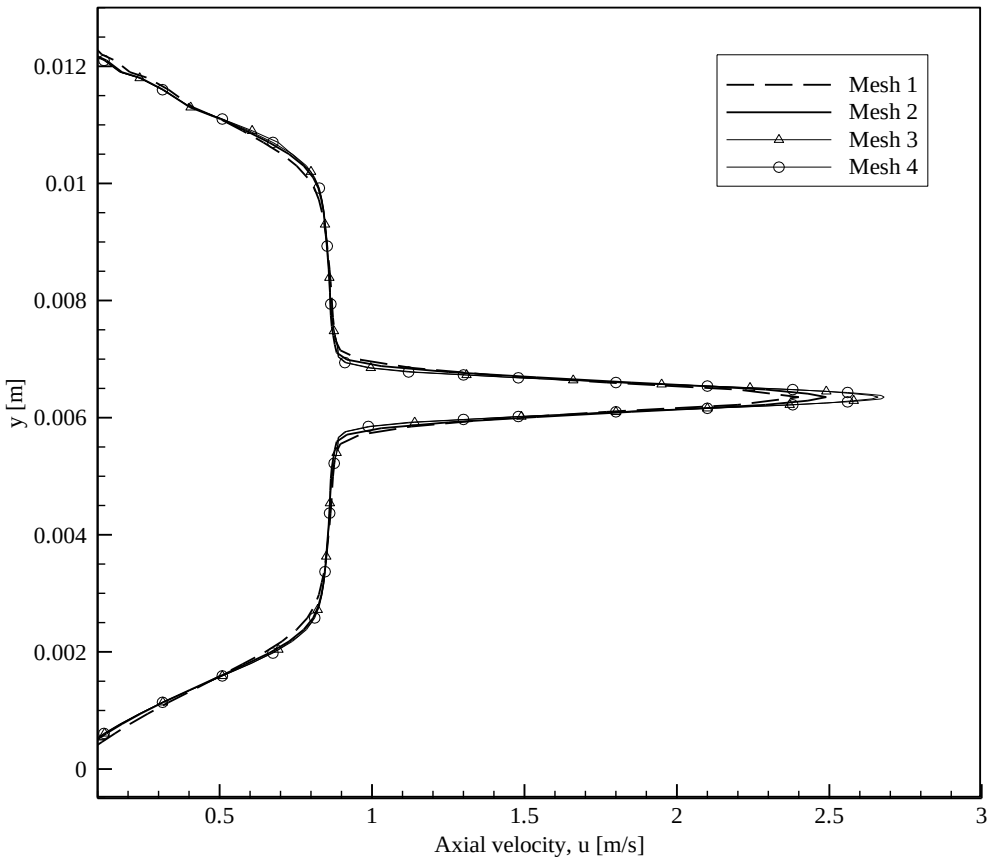

Figure 20. Axial velocity along vertical axis at x = 0.00127 m

Axial velocity distribution along x = 0.00127 m is tabulated in Table 13 and plotted in Figure 21.

Table 13. Mass fraction of methane along vertical axis at x = 0.00127 m

y [m]	Mass fraction of methane [ ]			
	Mesh 1	Mesh 2	Mesh 3	Mesh 4
0.000	0.0000	0.0000	0.0000	0.0000
0.001	0.0000	0.0000	0.0000	0.0000
0.003	0.0000	0.0000	0.0000	0.0000
0.005	0.0017	0.0003	0.0002	0.0002
0.006	0.4492	0.4681	0.5159	0.5221
0.008	0.0017	0.0003	0.0002	0.0002
0.010	0.0000	0.0000	0.0000	0.0000
0.011	0.0000	0.0000	0.0000	0.0000
0.013	0.0000	0.0000	0.0000	0.0000

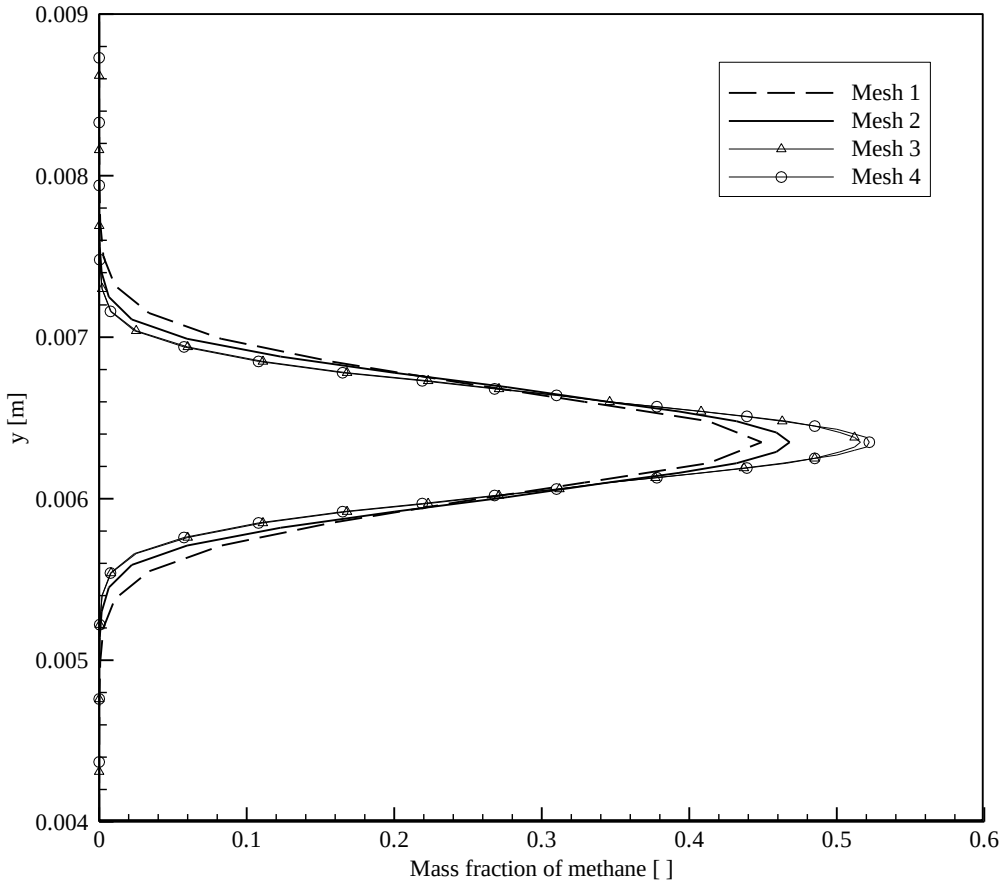

Figure 21. Mass fraction of methane along vertical axis at x = 0.00127 m

6.2.2.2. Reacting Flow

Similar to Non-reacting flow simulation, Ch-NR-I, different meshes are used to simulate reacting flow inside the Channel geometry. Mesh 1 is eliminated for this run and only the meshes which are stretched in both directions are used.

Table 14. Operating conditions and results for Run Ch-R-II

Run Number: Ch-R-II				RESULTS			
Mesh	m_f	m_o	P_o	P_{in}	m_o	V_o	T_o
	kg/s	kg/s	kPa	kPa	kg/s	m/s	K
Mesh 2	0.0009	0.026	10	10.0	0.0269	11.3	1639
Mesh 3	0.0009	0.026	10	10.0	0.0269	11.7	1784
Mesh 4	0.0009	0.026	10	10.0	0.0269	11.6	1765

Comparison of these three grids are done based on the axial velocity and temperature along centerline.

Axial velocity along centerline is tabulated in Table 15 and plotted in Figure 22.

Table 15. Axial velocity along centerline for Run Ch-R-II

x [m]	Velocity [m/s]		
	Mesh 2	Mesh 3	Mesh 4
0.000	5.37	5.37	5.35
0.005	5.64	5.57	5.58
0.010	6.09	5.89	5.88
0.015	6.87	6.56	6.53
0.020	7.74	7.36	7.32
0.025	8.58	8.17	8.13
0.030	9.34	8.94	8.89
0.036	10.00	9.64	9.59
0.041	10.50	10.26	10.23
0.046	11.16	11.04	11.02
0.051	13.85	13.78	13.78

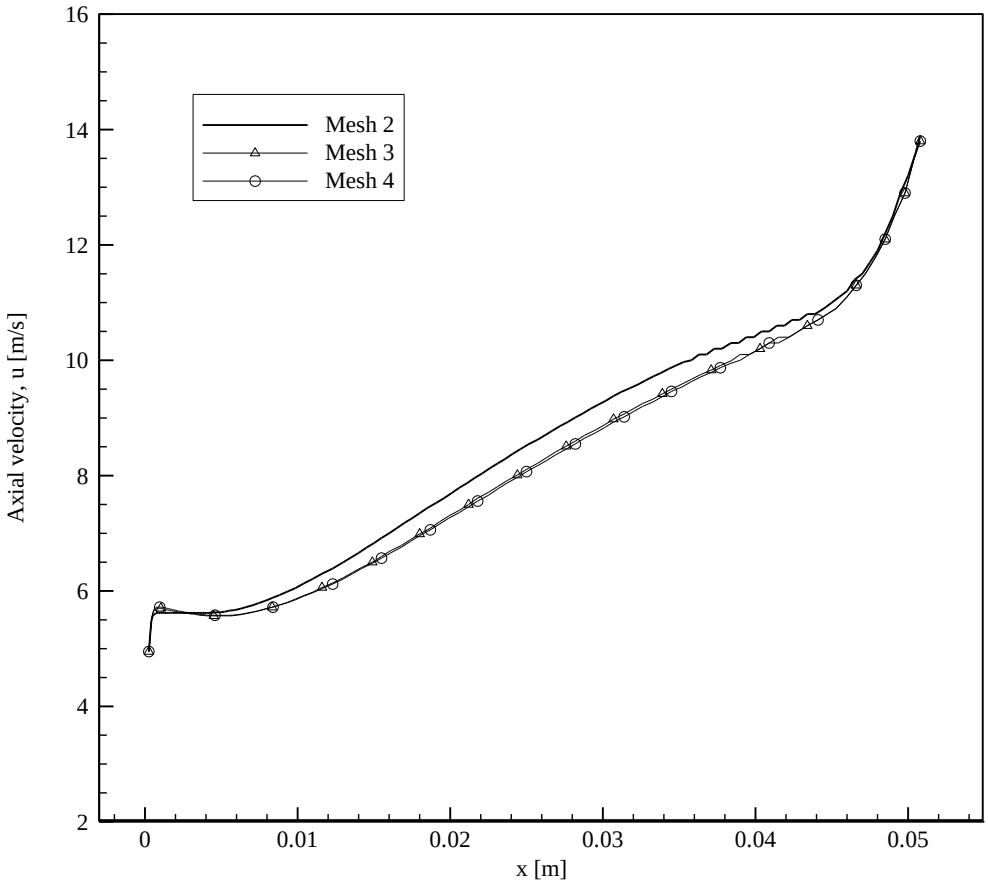

Figure 22. Axial velocity along centerline for Run Ch-R-II

Temperature along centerline is tabulated in Table 16 and plotted in Figure 23.

Table 16. Temperature along centerline for Run Ch-R-II

x [m]	Temperature [K]		
	Mesh 2	Mesh 3	Mesh 4
0.000	328.0	308.1	306.2
0.005	1163.9	1049.3	1038.9
0.010	1514.7	1378.5	1364.7
0.015	1770.8	1620.8	1604.6
0.020	2001.3	1845.9	1827.4
0.025	2205.8	2068.8	2050.5
0.030	2362.9	2261.3	2246.7
0.036	2463.4	2400.8	2391.0
0.041	2448.8	2472.5	2471.7
0.046	2358.4	2417.8	2425.2
0.051	2226.4	2289.1	2297.5

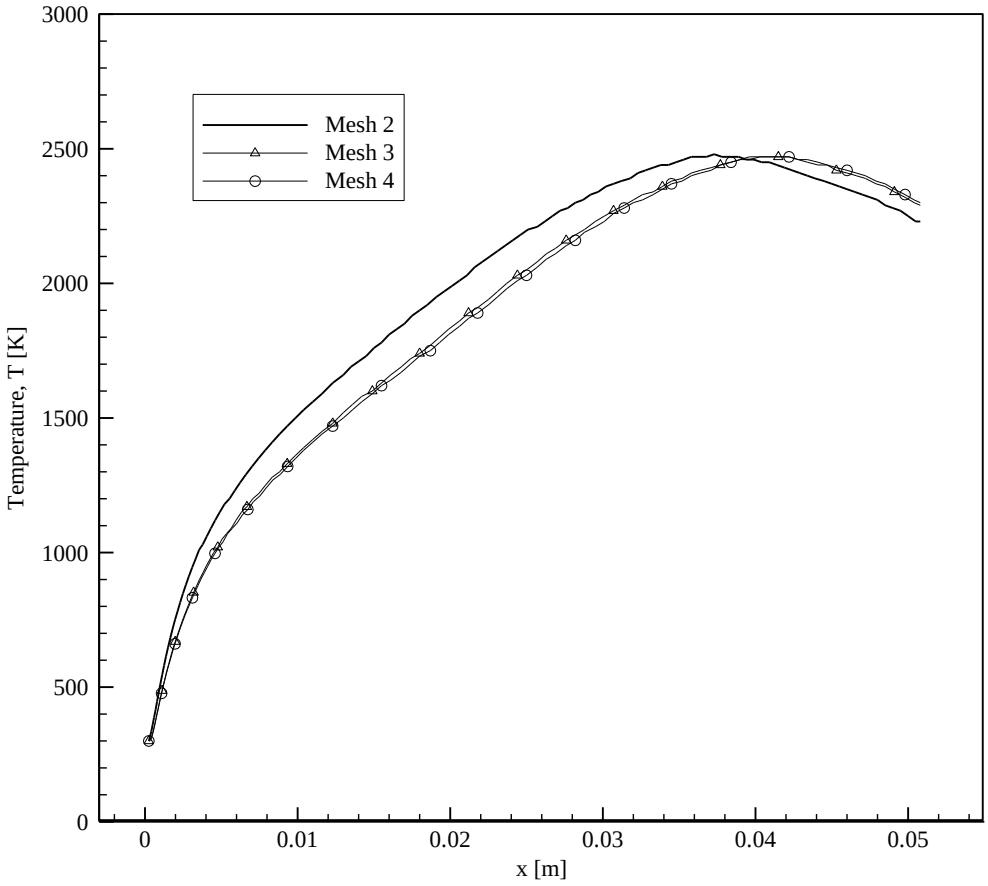

Figure 23. Temperature along centerline for different meshes

Based on the results presented in Sections 6.2.2.1 and 6.2.2.2, Mesh 3 is decided to be used in the following simulations since there are minor differences in the results of Mesh 3 and the finer mesh, Mesh 4.

6.3. Comparison of Computational and Experimental Results

Computational model is calibrated based on experimental data by modifying specific heats of combustion products, carbon dioxide and water vapor. Increasing specific heats provided more reasonable temperature distribution in LPRM especially at high temperatures. Specific heats of the products are taken as constant at two temperature bands differently. The suggested specific heats are:

$c_{p,CO2}$ = 1000 J/kg-K and $c_{p,H2O}$ = 1000 J/kg-K for 300 < T < 1000 K

$c_{p,CO2}$ = 2000 J/kg-K and $c_{p,H2O}$ = 5500 J/kg-K for 1000 < T < 5000 K

Although constant specific heat is not very reasonable approach for reacting flows, it provides idea about modifying specific heats. The specific heats of all species must be modified. Here, the results based on the proposed modified specific heats are presented.

Results of the computational simulations are compared to experimental data by temperature taken from the specific locations in the experiments. Second phase of the Run 1 (2nd Valve Setting) is selected for comparison. Operating conditions and the results for the computational simulation is presented in Table 17. In Table 18, the comparison of computational and experimental results is made and plotted in Figure 24. The experimental values of temperature presented in this table are for time, to t = 13:28:51.

Table 17. Operating conditions and results for CCNF-R-I

Run Number: CCNF-R-I			RESULTS				
m_f	m_o	P_o	P_{in}	m_o	V_o	RR	T_o
kg/s	kg/s	kPa	kPa	kg/s	m/s	kmol/ m^3s	K
0.0009	0.026	10	10.2	0.0269	35.7	26.1	1524

Table 18. Temperature values at thermocouple points

x [m]	Temperature [K]		% Difference
	CFD	Exp.	
0.00635	1070.6	986.41	8.53
0.01270	1472.3	1532.55	-3.93
0.01905	1688.7	1637.9	3.10

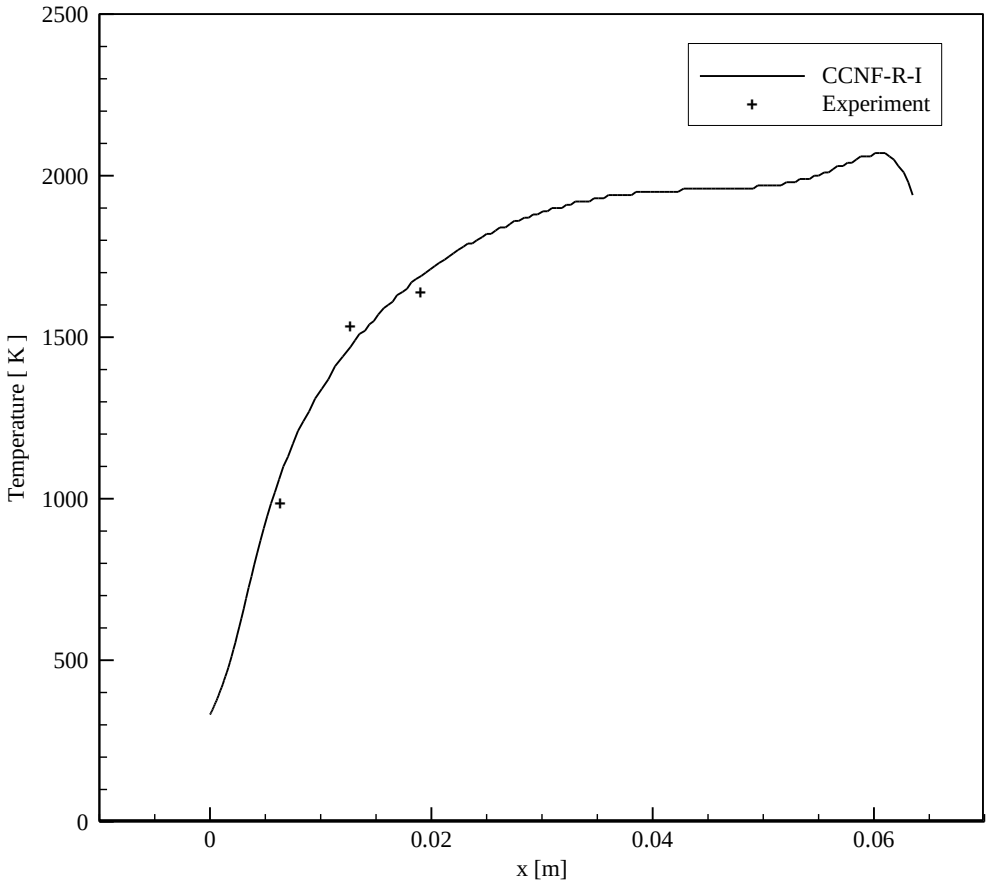

Figure 24. Temperature histogram at y = 0.15 along horizontal axis from Run CCNF-R-I compared with measured data from Run 1.

Through Figure 25 to Figure 31, temperature, pressure, density and mass fractions of methane and products are presented for the Base case study.

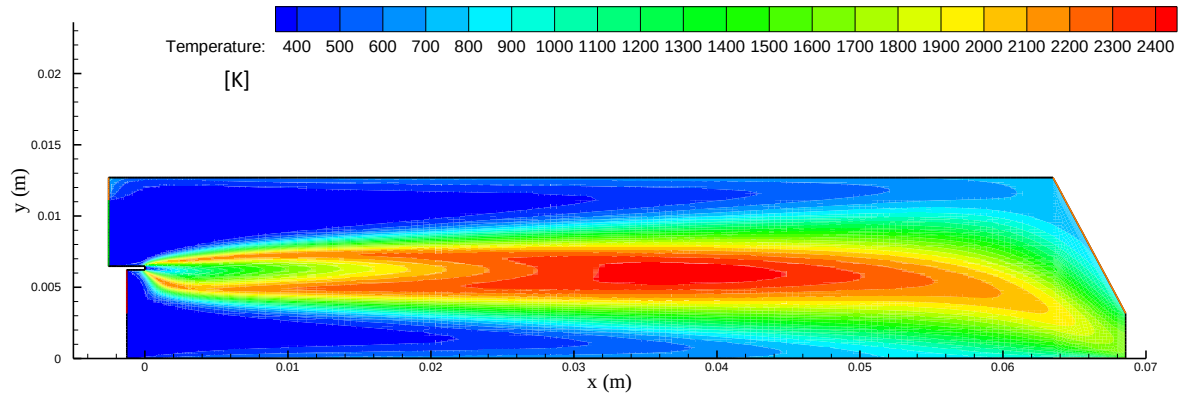

Figure 25. Temperature distribution (in Kelvins) inside CCFN for Run CCNF-R-I

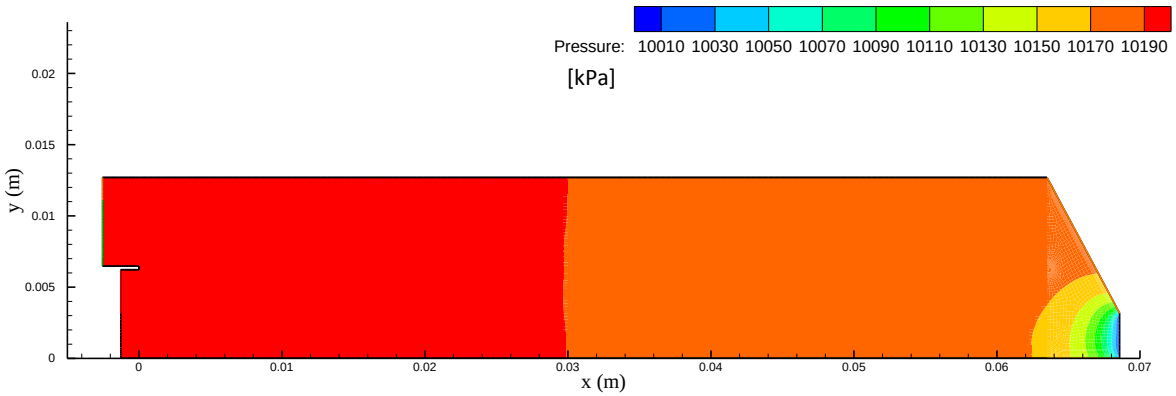

Figure 26. Pressure distribution (in Pascals) inside CCFN for Run CCNF-R-I

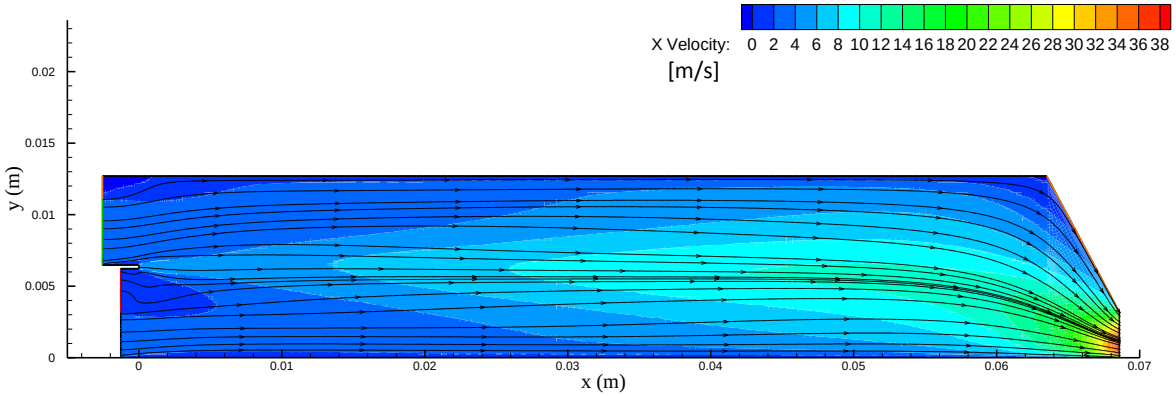

Figure 27. Predicted x-velocity (in m/s) inside CCFN for Run CCNF-R-I

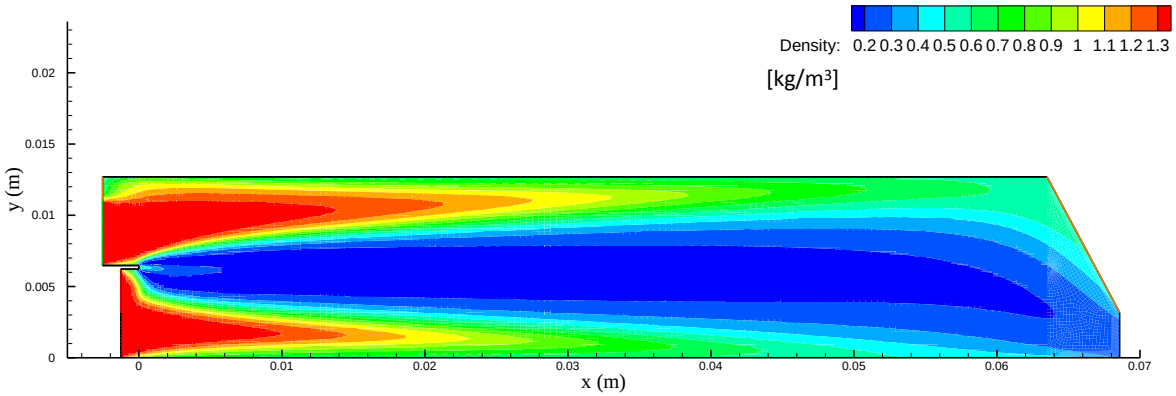

Figure 28. Density (in kg/m^3) variation inside CCFN for Run CCNF-R-I

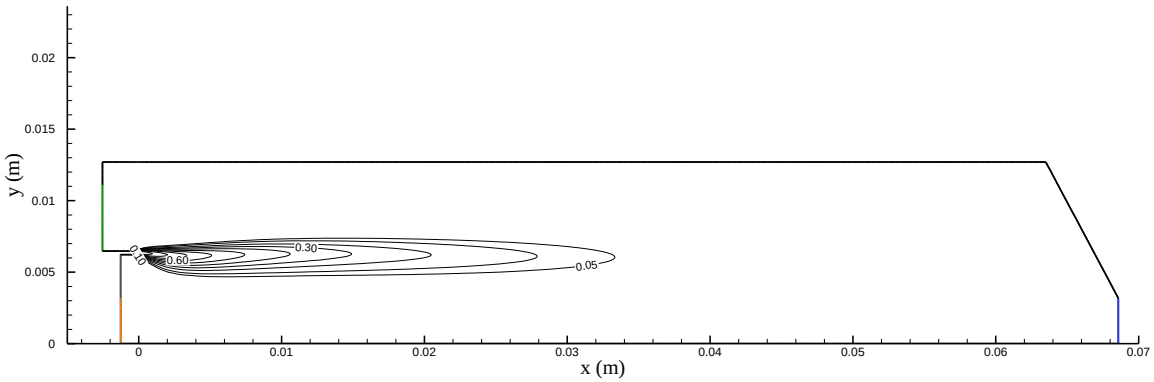

Figure 29. Mass fraction of CH_4 inside CCFN for Run CCNF-R-I

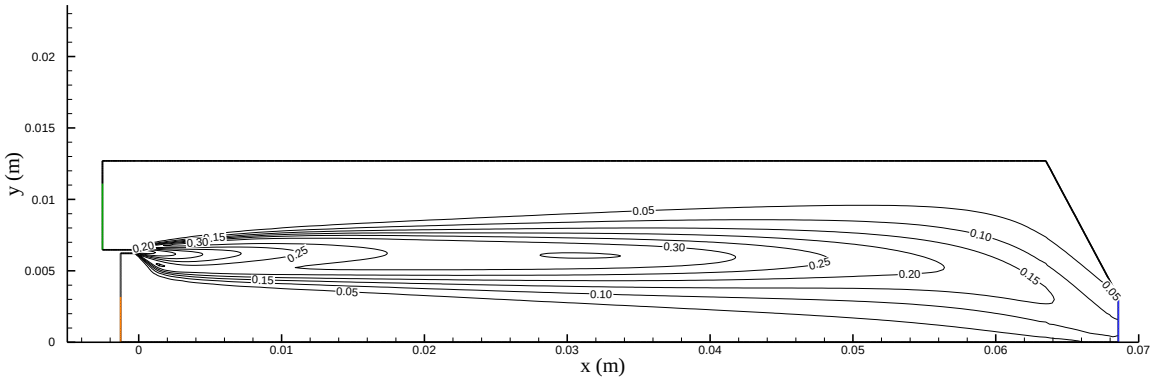

Figure 30. Mass fraction of CO_2 inside CCFN for Run CCNF-R-I

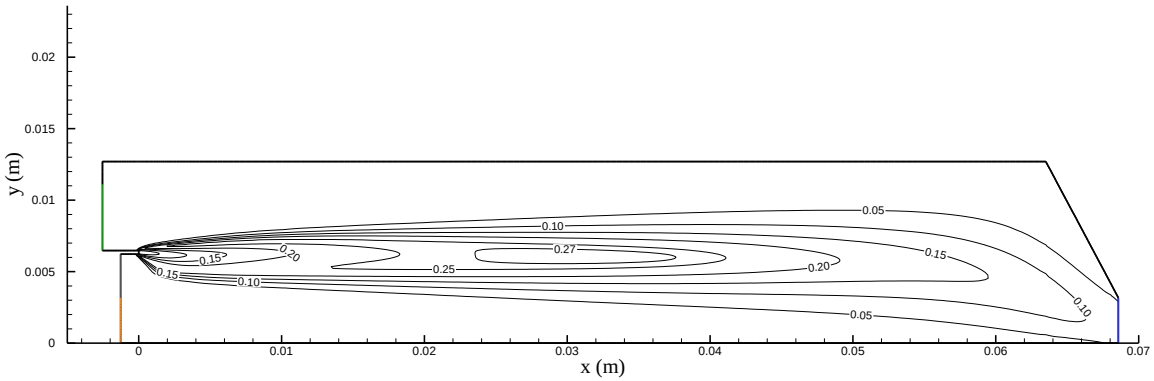

Figure 31. Mass fraction of H_2O inside CCFN for Run CCNF-R-I

As can be seen from Table 18 and Figure 24, computational results are in a good agreement with experimental results. In this section, the computational model is verified that gives

reasonable results. In the following sections of this thesis, effect of the several parameters are investigated in order to provide data to the design of combustion experiments in the future. Detailed list of the parameters used in Run CCFN-R-I can be found in Appendix VII.

6.4. Parametric Study

In this section, effects of several parameters are investigated on flow and combustion characteristics in order to provide insight for the experiments to be conducted in the near future. These parameters are mass flow rates of fuel and oxidizer and outlet pressure.

6.4.1. Effect of Different Mass Flow Rates

6.4.1.1. Effect of Fuel Mass Flow Rate

Operating conditions and results are presented in Table 19.

Table 19. Operating conditions and results for Run CCNF-R-II

Run Number: CCNF-R-II			RESULTS				
m_f	m_o	P_o	P_{in}	m_o	V_o	RR	T_o
kg/s	kg/s	kPa	kPa	kg/s	m/s	kmol/ m^3s	K
0.0005	0.026	10	10.1	0.0265	25.6	26.1	1124
0.0009	0.026	10	10.2	0.0269	35.7	26.6	1524
0.0015	0.026	10	10.3	0.0275	46.9	28.6	1919

In Figure 32, temperature distributions inside CCNF are presented for various fuel mass flow rates.

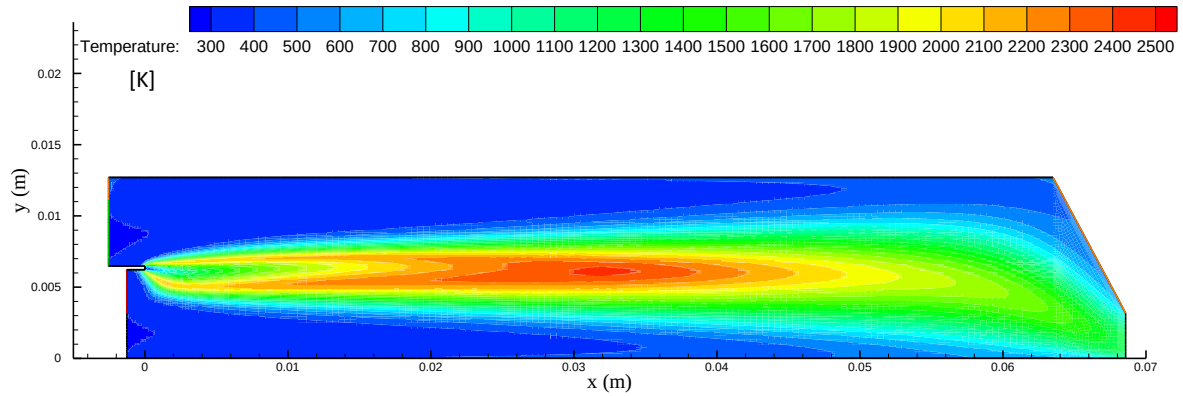

(a)

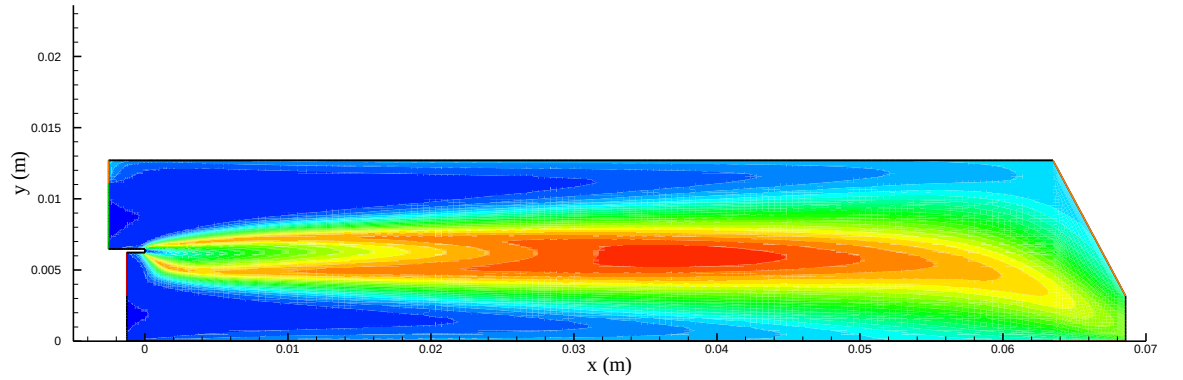

(b)

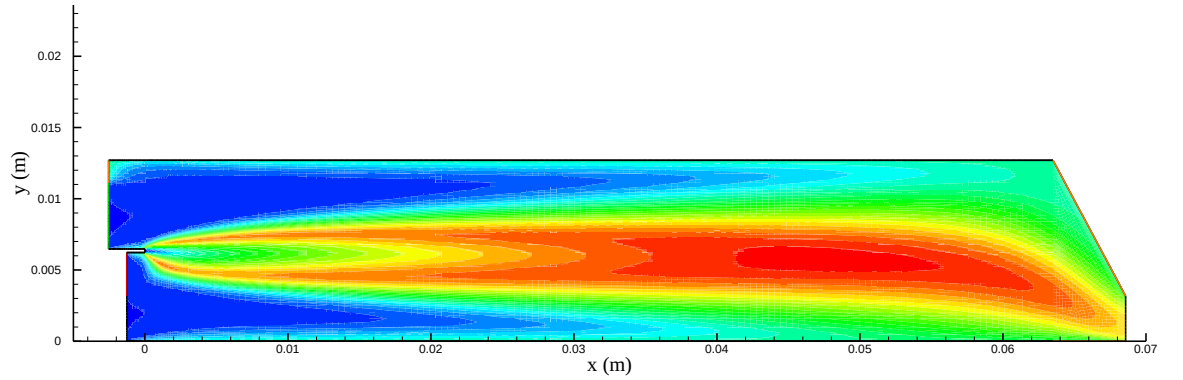

(c)

Figure 32. Temperature distribution (in Kelvins) inside CCNF for the Run CCNF-R-II. (a) $\dot{m}_f$ = 0.0005 kg/s, (b) $\dot{m}_f$ = 0.0009 kg/s, $\dot{m}_f$ = 0.0015 kg/s

As the mass flow rate of fuel increases, high temperature region of the flow moves through nozzle and mean temperature of the outflow increases. Although maximum

temperature inside CCNF does not change significantly, high temperature region gets bigger with the increasing fuel mass flow rate.

6.4.1.2. Effect of Oxidizer Mass Flow Rate

Operating conditions and results for Run CCNF-R-III are presented in Table 20.

Table 20. Operating conditions and results for Run CCNF-R-III

Run Number: CCNF-R-III			RESULTS				
m_f kg/s	m_o kg/s	P_o kPa	P_{in} kPa	m_o kg/s	V_o m/s	RR kmol/ m^3s	T_o K
0.0009	0.013	10	10.1	0.0139	25.7	28.8	2071
0.0009	0.026	10	10.2	0.0269	35.7	26.6	1524
0.0009	0.050	10	10.5	0.0509	44.6	22.6	1025

In Figure 33, temperature distributions inside CCNF are presented for various oxidizer mass flow rates.

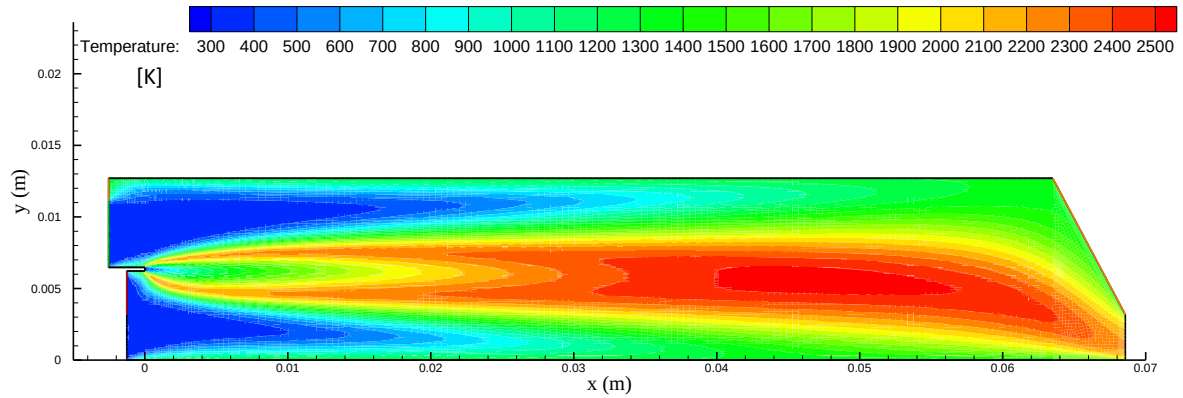

(a)

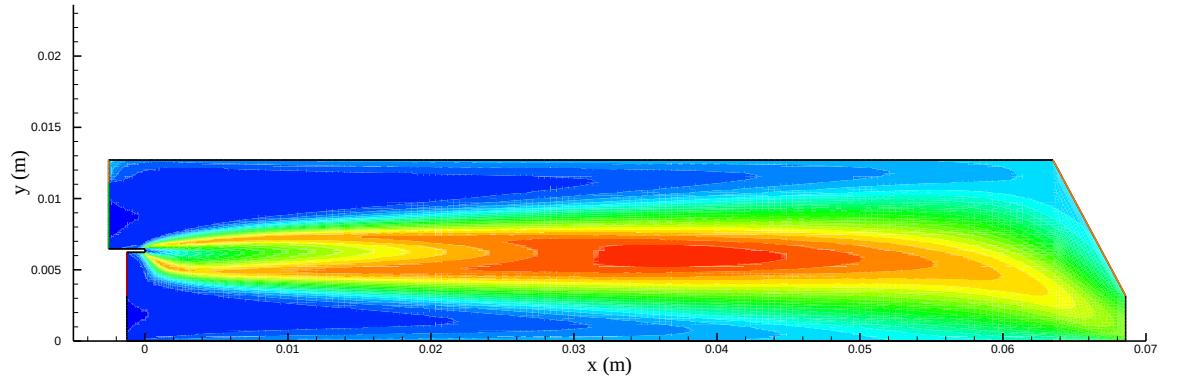

(b)

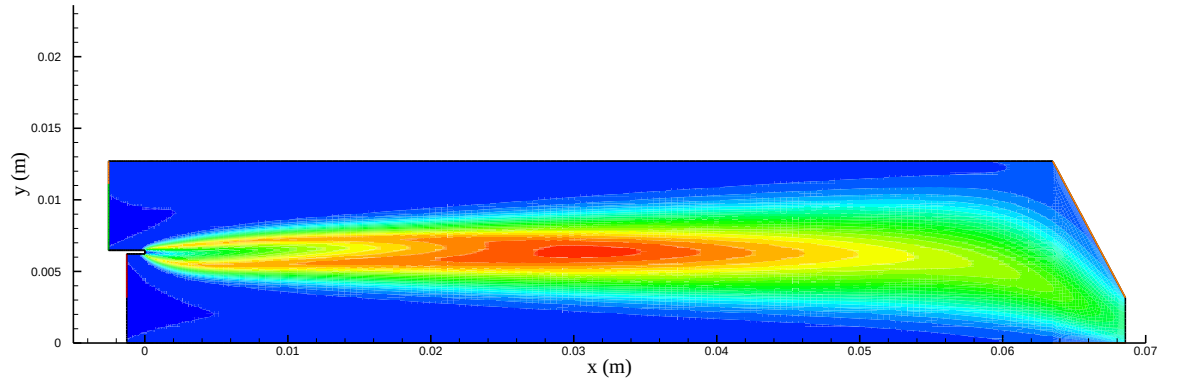

(c)

Figure 33. Temperature distribution (in Kelvins) inside CCNF for the Run CCNF-R-III. (a) $\dot{m}_{ox}$ = 0.013 kg/s, (b) $\dot{m}_{ox}$ = 0.026 kg/s, $\dot{m}_{ox}$ = 0.05 kg/s

Oxygen acts as a cooling agent as well as an oxidizer for the fuel. Therefore, by increasing oxidizer mass flow rate, chamber temperature can be decreased.

6.4.2. Effect of Different Outlet Pressures

Operating conditions and results for Run CCNF-R-III are presented in Table 21. Operating conditions and results for Run CCNF-R-I.

Table 21. Operating conditions and results for Run CCNF-R-IV

Run Number:			RESULTS				
m_f kg/s	m_o kg/s	P_o kPa	P_{in} kPa	m_o kg/s	V_o m/s	RR kmol/ m^3s	T_o K
0.0009	0.026	10	10.2	0.0269	35.7	26.6	1524
0.0009	0.026	100	100.1	0.0269	19.8	30.6	1525
0.0009	0.026	300	300.1	0.0269	9.9	32.7	1525

In Figure 34, temperature distributions inside CCNF are presented for various fuel mass flow rates.

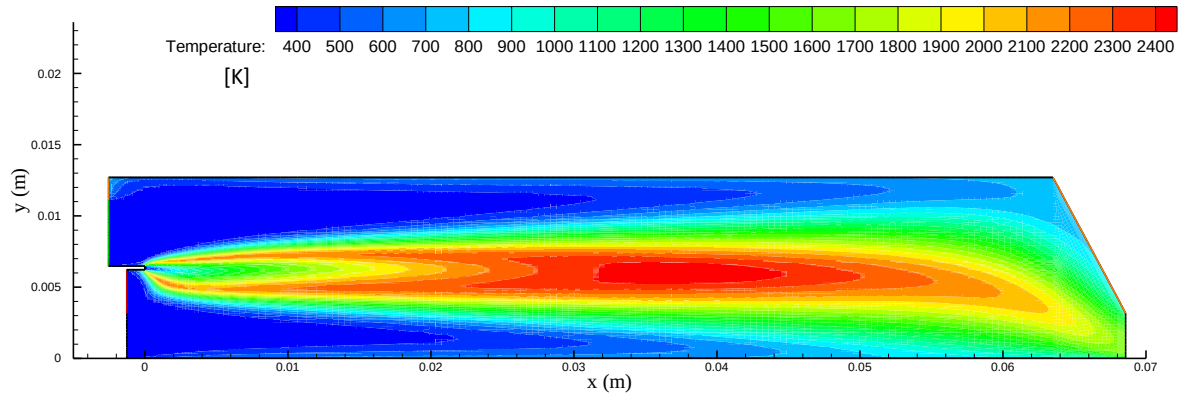

(a)

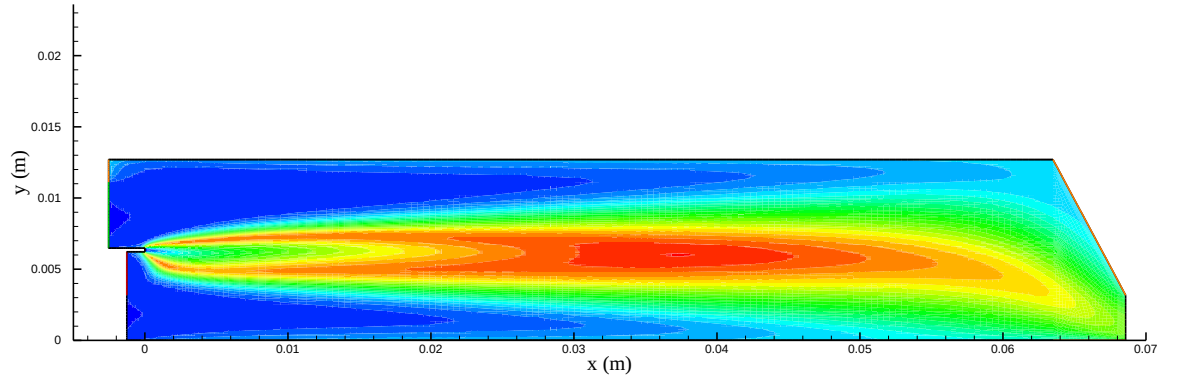

(b)

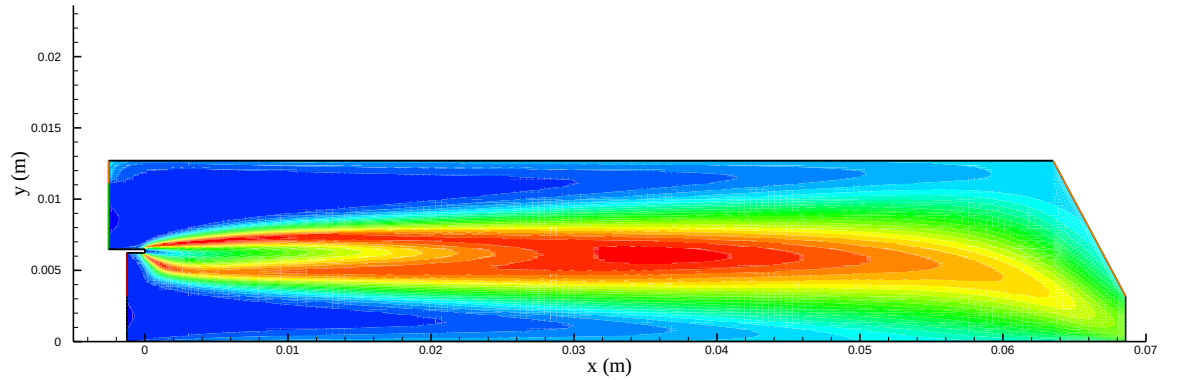

(c)

Figure 34. Temperature distribution (in Kelvins) inside CCNF for the Run CCNF-R-IV. (a) P_o = 10 kPa, (b) P_o = 100 kPa, (c) P_o = 300 kPa

As higher pressures are prescribed at outlet, pressure and density in the chamber increases. Therefore, pressure has an indirect effect of the characteristics of combustion. Higher reaction rates are attained with higher densities. Although maximum temperature does not change significantly, temperature gradient of gases inside chamber decreases.

7. CONCLUSIONS

In this thesis, the reacting flow inside the LPRM is studied experimentally and computationally. Experiments are conducted in University of New Orleans Combustion Laboratory. Computational simulation has been done using ANSYS Fluent as a solver. Flow inside the combustion chamber is modeled as viscous, turbulent and compressible in 2-D planar domain. Mathematical modeling is done based on unsteady assumption. In CFD simulations, pseudo – transient approach is utilized to determine steady – state temperature distribution. Benchmark cases for non-reacting and reacting flows are considered to verify the accuracy of the computational model. Four different mesh sizes are used for determination of the most proper grid considering the accuracy of solutions and computation time.

The following conclusions were drawn from the results of the simulations:

1. Benchmark case of flow between semi-infinite plates is taken and compared with the results found in the present study. Results shows that the present mathematical model gives accurate results for the Benchmark case considered.
2. A special solution procedure is constructed for the numerical simulations, which utilizes different reaction models. Results show that this procedure provides an accurate prediction for the location of chemical reaction as well as a reasonable temperature distribution of gases inside LPRM.
3. The computational model is calibrated in order to obtain a reasonable gas temperature distribution inside LPRM by modifying specific heats of products. After calibration, there is a good agreement between the results obtained from computational model and the experiments.

4. The results of the parametric study give idea about the effects of mass flow rates of fuel and oxidizer and pressure at outlet to design the future experiments for non – intrusive measurement of temperature with TDLAS.

8. RECOMMENDATIONS

This thesis aimed to understand the characteristics of reacting flow of methane and oxygen inside a low – pressure rocket motor. To improve the present study:

i. The base case CFD simulation is calibrated based on experimental results for temperature by modifying specific heats of combustion products, i.e. carbon dioxide and water vapor. Modification of specific heats should be according to the data in the literature.

ii. CFD simulations should be repeated for unsteady reacting flow of methane and oxygen.

REFERENCES

[1] E. Seedhouse, SpaceX: making commercial spaceflight a reality. Springer Science & Business Media, 2013.

[2] E. Seedhouse, Red Dragons, Ice Dragons, and the Mars Colonial Transporter. Springer International Publishing, 2016.

[3] K. M. Akyuzlu, H. Sayed, and Y. Pavri, "Determination of Regression Rate in Ablating Solid Fuels for Hybrid Rocket Motors Using a 2-D Subscale Low Pressure Test Bed," in Ankara International Aerospace Conference, 2005.

[4] P. Dagaut, J.-C. Boettner, and M. Cathonnet, "Methane Oxidation: Experimental and Kinetic Modeling Study," Combust. Sci. Technol., vol. 77, no. 1–3, pp. 127–148, 1991.

[5] G. B. Skinner, A. Lifshitz, K. Scheller, and A. Burcat, "Kinetics of Methane Oxidation," J. Chem. Phys., vol. 56, no. 8, pp. 3853–3861, 1972.

[6] F. N. Egolfopoulos, P. Cho, and C. K. Law, "Laminar flame speeds of methane-air mixtures under reduced and elevated pressures," Combust. Flame, vol. 76, no. 3–4, pp. 375–391, 1989.

[7] T. C. Wagner and C. R. Ferguson, "Bunsen flame hydrodynamics," Combust. Flame, vol. 59, no. 3, pp. 267–272, 1985.

[8] K. K. Kuo, Principles of Combustion. 1986.

[9] G. E. Andrews and D. Bradley, "The burning velocity of methane-air mixtures," Combust. Flame, pp. 275–288, 1972.

[10] D. D. S. Liu and R. MacFarlane, "Laminar burning velocities of hydrogen-air and hydrogen-air steam flames," Combust. Flame, vol. 49, no. 1–3, pp. 59–71, 1983.

[11] Y. C. Chen, N. Peters, G. a Schneemann, U. Wruck N. und Renz, and M. S. Mansour, "The Detailed Flame Structure of Highly Stretched Turbulent Premixed Methane-Air-Flames," Combust. Flame, vol. 107, pp. 223–244, 1996.

[12] H. Kobayashi, K. Seyama, H. Hagiwara, and Y. Ogami, "Burning velocity correlation of methane/air turbulent premixed flames at high pressure and high temperature," Proc. Combust. Inst., vol. 30, no. 1, pp. 827–834, 2005.

[13] S. Pfadler, M. L??ffler, F. Dinkelacker, and A. Leipertz, "Measurement of the conditioned turbulence and temperature field of a premixed Bunsen burner by planar laser Rayleigh scattering and stereo particle image velocimetry," Exp. Fluids, vol. 39, no. 2, pp. 375–384, 2005.

[14] B. A. V Bennett, C. S. McEnally, L. D. Pfefferle, and M. D. Smooke, "Computational and experimental study of axisymmetric coflow partially premixed methane/air flames," Combust. Flame, vol. 123, no. 4, pp. 522–546, 2000.

[15] K. M. Akyuzlu, “Modeling of Instabilities Due to Coupling of Acoustic and Hydrodynamic Oscillations in Hybrid Rocket Motors,” 43rd AIAA/ASME/SAE/ASEE Jt. Propuls. Conf. Exhib., no. July, pp. 1–11, 2007.

[16] K. M. Akyuzlu and K. Albayrak, “IMECE2011-64327 Thermal and Hydrodynamic Oscillations,” pp. 1–9, 2011.

[17] K. M. Akyuzlu, K. Albayrak, and C. Karaeren, “A Numerical Study of Thermoacoustic Oscillations in a rectangular Channel Using CMSIP Method,” in ASME 2009 International Mechanical Engineering Congress and Exposition, 2009.

[18] A. Antoniou and K. Akyuzlu, “A physics based comprehensive mathematical model to predict motor performance in hybrid rocket propulsion systems,” 41st AIAA/ASME/SAE/ASEE Jt. Propuls. Conf. Exhib. 10 - 13 July 2005, Tucson, Arizona, no. July, pp. 1–16, 2005.

[19] B. E. Launder and D. B. Spalding, Lectures in Mathematical Models of Turbulence. London: Academic Press, 1972.

[20] J. W. Rose, Technical Data on Fuels, 7th ed. Wiley, 1977.

[21] P. Cheng, “Two-Dimensional Radiating Gas Flow by a Moment Method,” AIAA J., vol. 2, pp. 1662–1664, 1964.

[22] R. Siegel and J. R. Howell, Thermal Radiation Heat Transfer. Washington D.C.: Hemisphere Publishing Corporation, 1992.

[23] H. Morihara and R. Ta-Shun Cheng, “Numerical solution of the viscous flow in the entrance region of parallel plates,” J. Comput. Phys., vol. 11, no. 4, pp. 550–572, 1973.

[24] Fluent, ANSYS FLUENT User ’ s Guide, vol. 15317, no. November. 2011.

[25] ANSYS FLUENT 13.0, Theory guide, vol. 15317, no. November. 2010.

APPENDIX – I

EQUIPMENT LIST USED IN THE EXPERIMENTS

Table I.1. LPRM Test Stand Equipment List

Item	Description	Brand	Model #	Serial #	Quantity
1	2" C-Clamp	-	-	-	3
2	2 ½" C-Clamp	-	-	-	2
3	3" C-Clamp	-	-	-	2
4	½" Control Valve	Worcestor	C466PMSE	-	3
5	Pressure Gauge	U. S. Gauges	-	-	3
6	Pressure Transducer	Omegadyne Inc.	PX02CI-200GV	135141	1
7	Pressure Transducer	Omegadyne Inc.	PX02CI-200GV	135147	1
8	Pressure Transducer	Precision Sensors	-	25828	1
9	Pressure Differential	Omega	PX 821-010DV	1503618	1
10	Pressure Regulator	Matheson	1H-350	-	1
11	Pressure Regulator	Matheson	1L-346	-	1
12	Pressure Regulator	Matheson	1L-580	-	1
13	Piezo Igniter	Char-Broil	-	-	1
14	Needle Valve	Swagelok			

Table I. 2. LPRM Data Acquisition (DAQ) Equipment List

Item	Description	Brand	Model #	Serial #	Quantity
1	ATD Board	National Instruments	PC1-M10-16XE-50		1
2	DAQ 4ft. Data Cable	National Instruments			1
3	DAQ Chassis Connection	National Instruments	SCXI-1349		1
4	Multiplex Amplifier 32-Channel	National Instruments	SCXI-1100		1
5	4-Channel Isolation Amp w/Excitation	National Instruments	SCXI-1121		1
6	8-Channel Thermocouple Amplifier	National Instruments	SCXI-1112		1

APPENDIX – II

CALIBRATION CURVES FOR THE EXPERIMENTS

MD2 CH0 Differential Pressure Transducer

Table II.1: Differential Pressure Transduer values taken to make a calibration curve.

Valve (rad)	Pressure Upstream (psig)	Pressure Downstream (psig)	Voltage (mV)	Delta P (psig)
0	40	40	0.01	0
π	40	40	0.03	0
2π	40	39.6	0.07	0.4
3π	40	39.1	0.12	0.9
4π	40	39.1	0.19	0.9
5π	40	38.6	0.28	1.4
6π	40	38.1	0.37	1.9
7π	40	38.1	0.49	1.9
8π	40	37.6	0.62	2.4
9π	39.9	37.1	0.76	2.8
10π	39.9	36.6	0.9	3.3
11π	39.9	36.1	1.05	3.8
12π	39.8	35.6	1.19	4.2

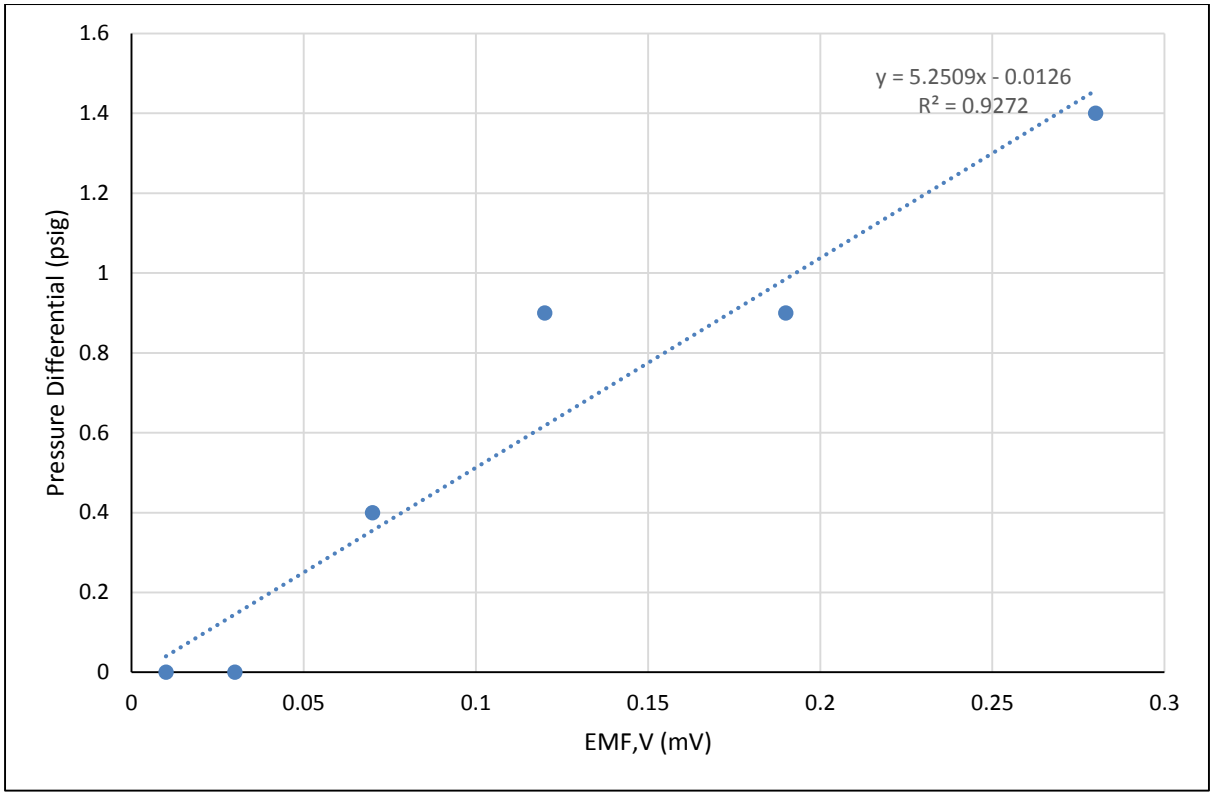

Figure II.1. Calibration Curve for Methane Inlet Differential Pressure Transducer. (Md. 2 Ch. 0)

MD2 CH3 Combustion Chamber Pressure Transducer

Table II.2: Pressure Transduer values taken to make a calibration curve.

EMF, V (mV)	Pressure, P (psig)
0.21	0
0.46	5
0.59	10
0.72	15
0.93	20
1.08	25
1.27	30
1.41	35
1.61	40

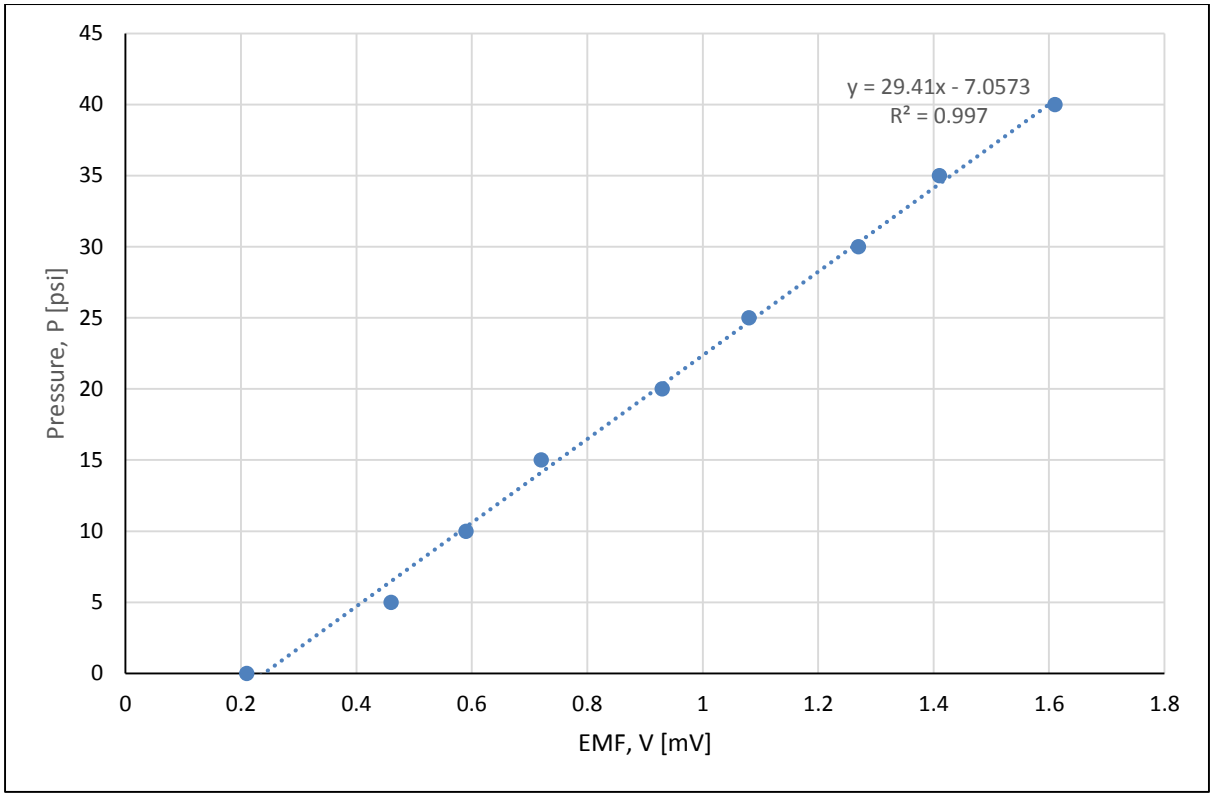

Figure II. 2. Calibration curve for Chamber Pressure Transducer (Md. 2 Ch. 3)

APPENDIX – III

CALCULATION OF THE FUEL MASS FLOW RATE

Equation $\dot{m}_{CH_4} = KA_2\gamma_1 Y\sqrt{2g_0(\frac{P_1\text{-}P_2}{\gamma_1})}$ *(15* can be used to determine the mass flow rate of methane.

$$\dot{m}_{CH_4} = KA_2\gamma_1 Y\sqrt{2g_0(\frac{P_1-P_2}{\gamma_1})} \quad (15)$$

where *K* is the flow coefficient and Y is the compressibility factor and defined in Equations 2 and 3.

$$Y = \left\{\left(\frac{P_2}{P_1}\right)^{\frac{2}{k}}\left(\frac{k}{k-1}\right)\left[\frac{1-\left(\frac{P_2}{P_1}\right)^{\frac{k-1}{k}}}{1-\left(\frac{P_2}{P_1}\right)}\right]\times\left[\frac{1-\left(\frac{A_2}{A_1}\right)^2}{1-\left(\frac{A_2}{A_1}\right)^2\left(\frac{P_2}{P_1}\right)^{\frac{2}{k}}}\right]\right\}^{\frac{1}{2}} \quad (16)$$

$$K = C\frac{1}{\sqrt{1-\left(\frac{A_2}{A_1}\right)^2}} \quad (17)$$

C is the discharge coefficient.

APPENDIX – IV

VECTOR FORM OF THE GOVERNING DIFFERENTIAL EQUATIONS

The continuity equation is given by:

$$\frac{D\rho}{Dt} + \rho\,\vec{\nabla}\cdot\vec{V} = 0 \tag{IV.1}$$

The momentum equations are given by:

$$\frac{D\left(\rho\vec{V}\right)}{Dt} = \vec{g} - \vec{\nabla}p + \frac{\partial}{\partial x_j}\left[\,\mu\left(\frac{\partial u_i}{\partial x_j} + \frac{\partial u_j}{\partial x_i}\right) - \frac{2}{3}\delta_{i,j}\frac{\partial u_k}{\partial x_k}\right)\right] \tag{IV.2}$$

where

$$\delta_{i,j} = \begin{cases} 1 & if \quad i=j \\ 0 & if \quad i\neq j \end{cases} \tag{IV.3}$$

Transport equations for Standard k-ε model are given by:

$$\frac{D\left(\rho k\right)}{Dt} = \frac{\partial}{\partial x_j}\left(\left(\mu + \frac{\mu_t}{Pr_k}\right)\frac{\partial k}{\partial x_j}\right) - \mu_t\left(\frac{\partial u_i}{\partial x_j} + \frac{\partial u_j}{\partial x_i}\right)^2 + \rho\varepsilon = 0 \tag{IV.4}$$

$$\frac{D\left(\rho\varepsilon\right)}{Dt} = \frac{\partial}{\partial x_j}\left(\left(\mu + \frac{\mu_t}{Pr_\varepsilon}\right)\frac{\partial \varepsilon}{\partial x_j}\right) - C_{\varepsilon 1}\frac{\varepsilon}{k}\mu_t\left(\frac{\partial u_i}{\partial x_j} + \frac{\partial u_j}{\partial x_i}\right)^2 + \rho C_{\varepsilon 2}\frac{\varepsilon^2}{k} = 0 \tag{IV.5}$$

The energy equation is given by:

$$\frac{D\left(\rho e\right)}{Dt} + p\vec{\nabla}\cdot\vec{V} = \vec{\nabla}\cdot\left(k\,\vec{\nabla}T\right) + \Phi + \frac{\partial Q_s}{\partial t} \tag{IV.6}$$

The equation of state is:

$$p = \rho R T \tag{I.7}$$

And transport equation for species transport is given as:

$$\frac{D\left(\rho Y_i\right)}{Dt} = -\vec{\nabla}\cdot\vec{J}_i + R_i \tag{IV.8}$$

APPENDIX – V

LOG SHEETS OF EXPERIMENTS

Low Pressure Rocket Motor

Log Book

Date of Experiment: 9-12-15

Type of Procedure: Hot Test

Experiment Number: Run 1

Crew Present: Dr. Akyuzlu, Paul Fuller, Mine Kaya

Data Files:

1. PC Name:
2. Username:
3. File Folder Location:

Objective: To measure the temperature within the combustion chamber at three separate zones of the methane flame.

Operating Parameters:

	Gas	Tank Regulator Setting	Needle Valve Ignition Setting	Needle Valve Steady State Setting	
Fuel:	Methane	40 psig	10°	10°	5°
Oxidizer:	Oxygen	40 psig	20°	20°	10°
Purge:	Nitrogen	40 psig	0°	0°	0°

Preparation Check List:

1. Data Acquisition System: Settings □ Logging □
2. Gas Line Pressurized: Fuel □ Oxidizer □ Purge □
3. Thermocouples: MD4 Ch0 □ MD4 Ch1 □ MD4 Ch2 □ MD4 Ch3 □ MD 4 Ch4 □ MD4 Ch5 □ MD4 Ch6 □
4. Pressure Transducers: MD2 Ch0 □ MD2 Ch3 □

Time of Start: 27:01.4 End: 30:34.7

Recorder:

1. Tape Name: Time of Start: End:
2. DAQ File: Time of Start: End:

Observations:

Remarks:

Low Pressure Rocket Motor

Log Book

Date of Experiment:

Type of Procedure: Hot Test

Experiment Number: Run 2

Crew Present: Dr. Akyuzlu, Paul Fuller, Mine Kaya

Data Files:

4. PC Name:
5. Username:
6. File Folder Location:

Objective: To measure the temperature within the combustion chamber at three separate zones of the methane flame.

Operating Parameters:

	Gas	Tank Regulator Setting	Needle Valve Ignition Setting	Needle Valve Steady State Setting	
Fuel:	Methane	40 psig	10°	10°	5°
Oxidizer:	Oxygen	40 psig	20°	20°	10°
Purge:	Nitrogen	40 psig	0°	0°	0°

Preparation Check List:

5. Data Acquisition System: Settings □ Logging □
6. Gas Line Pressurized: Fuel □ Oxidizer □ Purge □
7. Thermocouples: MD4 Ch0 □ MD4 Ch1 □ MD4 Ch2 □ MD4 Ch3 □ MD 4 Ch4 □ MD4 Ch5 □ MD4 Ch6 □
8. Pressure Transducers: MD2 Ch0 □ MD2 Ch3 □

Time of Start: 39:40.7 End: 41:40.1

Recorder:

3. Tape Name: Time of Start: End:
4. DAQ File: Time of Start: End:

Observations:

Remarks:

APPENDIX – VI

RESULTS OF RUN 2

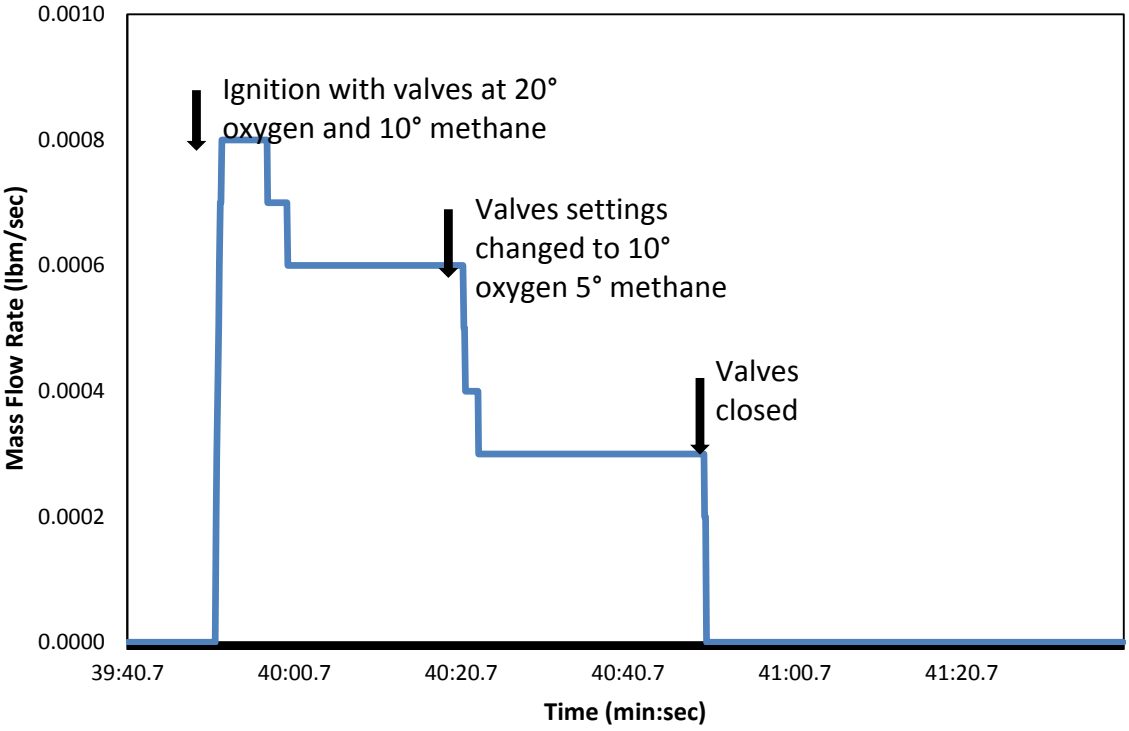

Figure VII.1. Mass flow rate for Run 2.

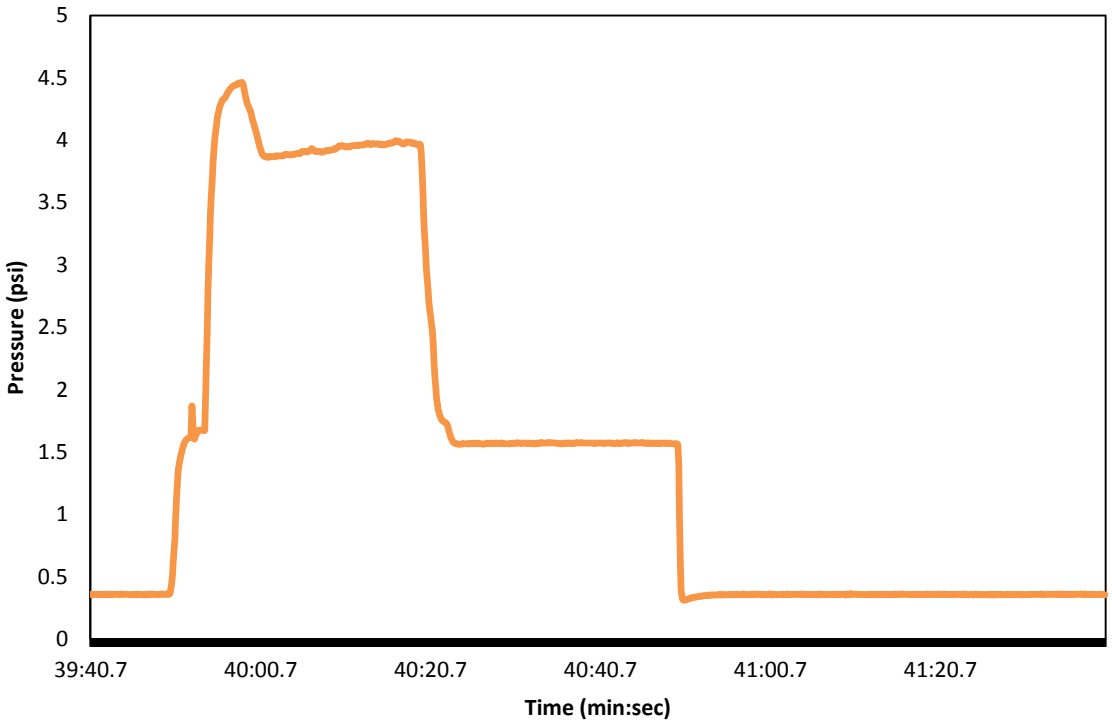

Figure VII.1. Chamber pressure for Run 2.

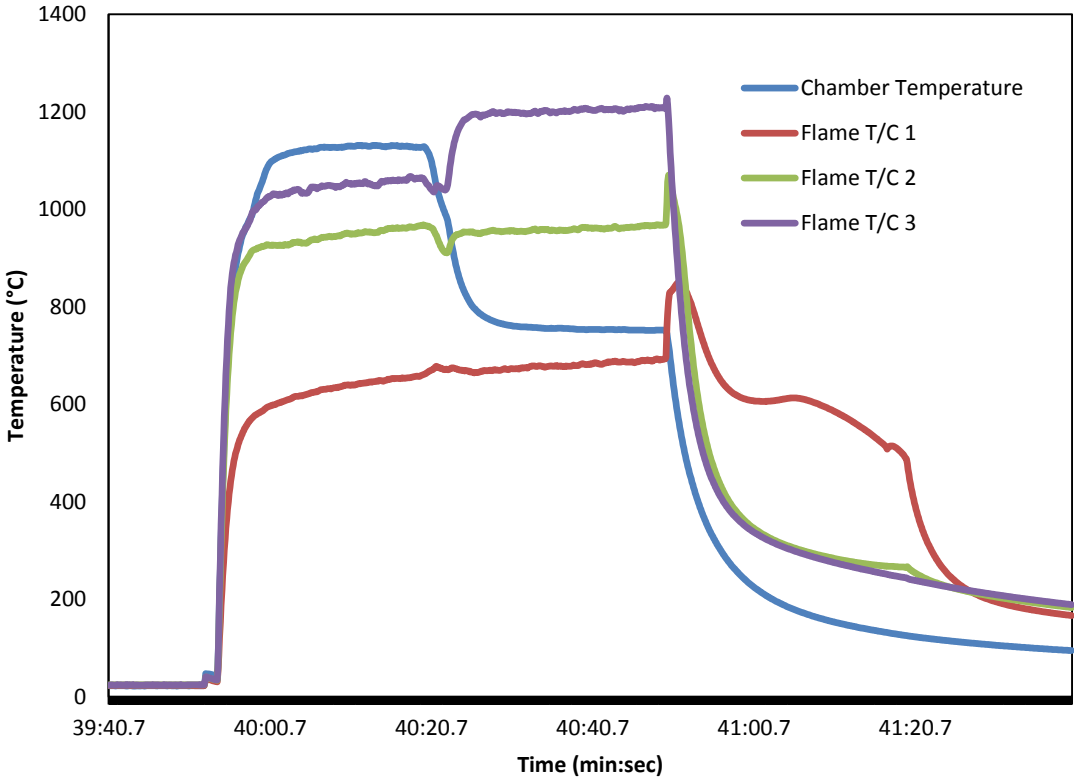

Figure VII.1. Recorded temperatures for Run 2.

APPENDIX – VII

PARAMETERS FOR THE BASE CASE (CCNF-R-I) SIMULATION

GEOMETRICAL PARAMETERS			
Parameter	**Symbol**	**Value**	**Unit**
Height of combustion chamber	H	0.5	inch
Length of combustion chamber	L_{CC}	2	inch
Length of mixing chamber (AFT)	L_{AFT}	0.5	inch
Height of fuel inlet	h_{fi}	0.01	inch
Height of oxidizer	h_{oi}	0.25	inch
Height of outlet	h_o	0.125	inch
Width	w	1.5	inch

OPERATIONAL PARAMETERS			
Parameter	**Symbol**	**Value**	**Unit**
Given			
Mass flow rate of fuel	m_f	0.0009	kg/s
Mass flow rate of primary oxidizer	m_{o1}	0.015	kg/s
Mass flow rate of secondary oxidizer	m_{o2}	0.011	kg/s
Temperature of fuel and oxidizer	T_{in}	300	K
Calculated			
Reynolds number at fuel inlet	Re_f	95.7	-
Reynolds number at fuel inlet	Re_{ox}	2840	-
Reynolds number at outlet	Re_o	3498	-
Mach number at outlet	Ma_o	0.05	-

COMPUTATIONAL PARAMETERS			
Residuals Criteria (Non Reacting)	-	10^{-15}	-
(Reacting)	-	10^{-10}	-
Combustion Chamber & FWD (CCF)			
Number of nodes in x-direction	N_x	170	-
Number of nodes in y-direction	N_y	88	-
Stretching factor	SF	1.1	-
Minimum cell length in x direction	Δx_{min}	0.002	inch
Minimum cell length in y direction	Δy_{min}	0.0025	inch
Nozzle (N)			
Number of nodes	N_n	2563	-
Stretching factor	SF	1.1	-

PHYSICAL PARAMETERS			
Physical Parameters of Methane - Oxygen Mixture			
Parameter	**Symbol**	**Value**	**Unit**
Thermal conductivity	k	0.0454	W/m-K
Viscosity	μ	1.72 e-5	kg/m-s
Mass diffusivity	D	2.88 e-5	m^2/s

PHYSICAL PARAMETERS							
Coefficients of the Polynomial for the specific heat of substances ($c_p = C_1 + C_2\,T + C_3\,T^2 + C_4\,T^3 + C_5\,T^4$)							
		C1	C2	C3	C4	C5	
Methane	CH_4	403.58	9.06	-0.01443	$1.58\cdot10^{-5}$	$-6.34\cdot10^{-9}$	300 < T < 1000
		872.47	5.31	-0.00201	$3.52\cdot10^{-7}$	$-2.33\cdot10^{-11}$	1000 < T < 5000
Oxygen	O_2	834.83	0.29	-0.00015	$3.41\cdot10^{-5}$	$-2.28\cdot10^{-10}$	300 < T < 1000
		960.75	0.16	$-3.27\cdot10^{-5}$	$4.61\cdot10^{-9}$	$-2.95\cdot10^{-13}$	1000 < T < 5000
Nitrogen	N_2	979.04	0.42	-0.00118	$1.67\cdot10^{-6}$	$-7.26\cdot10^{-10}$	300 < T < 1000
		868.62	0.44	-0.00017	$3.00\cdot10^{-8}$	$-2.00\cdot10^{-12}$	1000 < T < 5000
Carbon dioxide	CO_2	1000					300 < T < 1000
		4000					1000 < T < 5000
Water Vapor	H_2O	2000					300 < T < 1000
		5500					1000 < T < 5000

TURBULENCE PARAMETERS			
Parameter	**Symbol**	**Value**	**Unit**
Turbulent viscosity coefficient	$C\mu$	0.09	-
Empirical constant 1	$C_{\varepsilon 1}$ *1*	1.44	-
Empirical constant 2	$C_{\varepsilon 2}$	1.92	-
Turbulent Prandtl number for k	Pr_k	1	-
Turbulent Prandtl number for eps	Pr_ε	1.3	-

COMBUSTION PARAMETERS			
Parameter	**Symbol**	**Value**	**Unit**
Stoichiometric coefficient for CH_4	v_{CH4}	1	-
Stoichiometric coefficient for O_2	v_{O2}	2	-
Stoichiometric coefficient for CO_2	v_{CO2}	1	-
Stoichiometric coefficient for H_2O	v_{H2O}	2	-
Rate exponent for methane	η_{CH4}	0.2	
Rate exponent for oxygen	η_{CH4}	1.3	
Pre-exponential factor	A_r	$2.119\cdot10^{11}$	
Activation Energy	E_r	$2.03\cdot10^{8}$	J/kg-mol

Vita

Mine Kaya was born on July 23, 1989 in Ankara, Turkey. She completed her Bachelor studies in mechanical engineering at Middle East Technical University (METU) in 2012. After working as a research and development engineer in industry for one year and a teaching assistant in the Department of Mechanical Engineering at METU, she was admitted to the Department of Mechanical Engineering at the University of New Orleans as a graduate research assistant. She has worked in the research project funded by NASA EPSCoR and Board of Regents. She received her Master of Science degree from the Department of Mechanical Engineering at University of New Orleans in August 2016.